Geochemistry, Geophysics, Geosystems®

RESEARCH ARTICLE
10.1029/2025GC012418

Abundant Ancient Melt-Depleted Peridotite Beneath the Marion Rise, Southwest Indian Ocean, Effects on Basalt Composition and Dynamic Topography

Dominic Woelki[1,2], Vincent Salters[1], Andreas Stracke[3], Felix Genske[3], Gary White[1], and Daniele Brunelli[4]

[1]National High Magnetic Field Laboratory and Department of Earth, Ocean and Atmospheric Science, Florida State University, Tallahassee, FL, USA, [2]Now at: Institute of Earth and Environmental Sciences, University of Freiburg, Freiburg im Breisgau, Germany, [3]Institüt für Mineralogie, Universität Münster, Münster, Germany, [4]Dipartimento di Scienze Chimiche e Geologiche, Università di Modena e Reggio Emilia, Modena, Italy

Key Points:

- Marion Rise peridotites show highly radiogenic Hf isotopes indicating ancient depletion
- Variations in the Hf-isotopic compositions of basalts show that they contain a melt component from anciently depleted peridotites
- The composition of the peridotites supports the assessment that the Marion Rise is mostly a density and not a temperature anomaly

Supporting Information:

Supporting Information may be found in the online version of this article.

Correspondence to:

V. Salters,
salters@magnet.fsu.edu

Citation:

Woelki, D., Salters, V., Stracke, A., Genske, F., White, G., & Brunelli, D. (2025). Abundant ancient melt-depleted peridotite beneath the Marion Rise, Southwest Indian Ocean, effects on basalt composition and dynamic topography. *Geochemistry, Geophysics, Geosystems*, *26*, e2025GC012418. https://doi.org/10.1029/2025GC012418

Received 6 MAY 2025
Accepted 17 AUG 2025

Author Contributions:

Conceptualization: Vincent Salters
Formal analysis: Dominic Woelki, Vincent Salters, Felix Genske
Funding acquisition: Vincent Salters, Andreas Stracke
Investigation: Dominic Woelki, Vincent Salters
Methodology: Dominic Woelki, Vincent Salters, Felix Genske, Gary White
Project administration: Vincent Salters
Resources: Felix Genske, Gary White, Daniele Brunelli
Software: Andreas Stracke

Abstract The Marion Rise (MR) at the central Southwest Indian Ridge (SWIR) is an ultra-slow spreading ridge with thin crust, shallow ridge depth, sparse basaltic coverage, and exposed peridotite. Clinopyroxenes from the MR peridotites have highly variable Hf-Nd isotopic composition extending to extreme ε_{Nd} of 94 and ε_{Hf} of 417, which requires extensive melting and evolution with high Lu/Hf for more than 1 Ga. The Yb content of clinopyroxenes is negatively correlated with the Cr# (molar Cr/Cr + Al) of spinel, but not with ε_{Hf}, indicating a multi-stage evolution of depletion and melt-rock reaction. The highly variable Hf-Nd isotopic compositions of the MR basalts are not systematically correlated and range from ε_{Nd} −8 to 9.1 and ε_{Hf} −10 to 32. Therefore, the basalts are probably a mixture of melts from several lithologies, for example, a recycled crustal component with exceptionally low Hf-Nd isotope ratios, in addition to melts from the volumetrically predominant, isotopically highly variable peridotites. The ancient melt-depletion of the MR peridotites with high Hf isotope ratios also reduced their density. A peridotitic mantle melted to <10% can support the Marion Rise without the need of increased mantle temperature. Ultra-depleted peridotites like those from the MR ones have been documented at multiple localities, indicating that they are ubiquitous in the sub-ridge mantle. Hence, melts from such ultra depleted peridotite influences mid-ocean ridge basalt (MORB) compositions and variably melt depleted sub-ridge peridotites should be considered when evaluating ridge depth variations.

Plain Language Summary Radiogenic hafnium and neodymium isotopic compositions of abyssal peridotites from the Marion Rise in the central Southwest Indian Ocean reveal a complex history, including partial melting that occurred more than a billion years ago. Because of their prior melt- and incompatible element depletion, however, melts from these depleted peridotites have only a subtle, but detectable, influence on the composition of the basalts. The isotopic composition of basalts at the Marion Rise is highly variable in composition and although they have significantly lower Nd and Hf isotope ratios than the peridotites, they show a significant imprint of melts from melts from the ancient, melt-depleted peridotites with much higher Hf and Nd isotope ratios. The ancient-melt depleted peridotites (like the ones at the Marion Rise) have also reduced density relative to "typical" mantle. If the peridotitic mantle has melted to 10% or more, it becomes light enough to support the Marion Rise without the need for increased mantle temperature. Therefore, the shallow depth of the Marion Rise is most likely due to a density rather than a temperature anomaly. Melt-depleted peridotites with low density and high Hf isotope ratios have been found at multiple locations along the global ridge system, indicating that such peridotites are ubiquitous and that they should be considered when evaluating variations in ridge depth and ridge basalt compositions.

1. Introduction

Ocean rises such as Iceland, Azores, and Galapagos are major topographic swells along mid-ocean ridges. These rises may result from the flow of hot mantle toward the mid-ocean ridge (Morgan, 1971, 1972), resulting in higher mantle temperature, thick crust, and elevated topography. This hypothesis has been supported by Dick et al. (1984), who showed that basalt chemistry correlates with ridge depth and the degree of melt–depletion of the associated abyssal peridotites. Klein and Langmuir (1987), found a correlation between decreasing Na8 in MORB (Na8 = Na_2O corrected for fractionation to 8 wt.% MgO) and increasing Fe8 (FeO corrected for fractionation to 8 wt.% MgO) with ridge depth on a global scale. O'Neill and Jenner (2016) showed, however, that using a larger

Supervision: Vincent Salters
Validation: Vincent Salters, Daniele Brunelli
Writing – original draft: Dominic Woelki
Writing – review & editing: Dominic Woelki, Vincent Salters, Andreas Stracke, Felix Genske, Daniele Brunelli

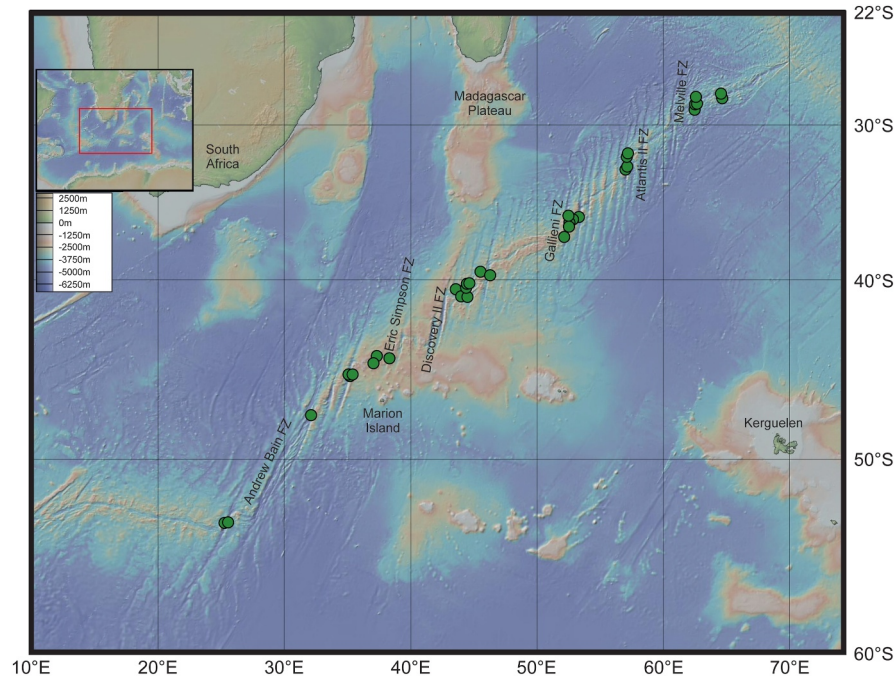

Figure 1. Location map of location of samples analyzed in this study (green dots).

collection of MORB data (Gale et al., 2013), the Na8-Fe8 correlation breaks down if anomalously deep or shallow ridges segments are excluded. MORB compositions, crustal thickness, and ridge depth, however, can also vary due to initial variations in upper mantle composition, with a melt-depleted and thus light, buoyant peridotite supporting shallow sections along mid-ocean ridges (Niu & O'Hara, 2008; O'Hara, 1965; Presnall & Helsley, 1982; Stracke, 2021). One example is the Marion Rise, that is, the stretch of the SWIR between the Andrew Bain Fracture Zone (ABFZ) at 32.5°E and the Gallieni FZ at approximately 53°E. Here, the crust is thin at the Marion Rise and mantle peridotite is exposed along the ridge, which shallows from ∼4 to 1.5 km depth at approximately 37°E–38°E. Zhou and Dick (2013) argued that the shallow depth of the Marion Rise is dynamically supported by buoyant melt-depleted peridotite. Hence, the Marion Rise is an ideal location to further examine the relationship between ridge depth, MORB composition, and crustal thickness. The setting is unique in that there are significant mantle exposures along the ridge. Furthermore, across the Andrew Bain Fracture Zone, the Pb and Hf isotope ratios change systematically and are inferred to represent the boundary between the Atlantic Ocean basin and Indian Ocean basin MORB (Dupré & Allègre, 1983; Mahoney et al., 1992). Basalts from the Indian Ocean ridges have an elevated Hf isotopic composition compared to Atlantic and Pacific MORB (Janney et al., 2005).

Here, we present chemical and isotopic data of abyssal peridotites from the eastern part of the SWIR and compare the peridotite compositions to previously published and new MORB data with the goal of understanding how mantle composition influences mantle melting, ridge depth and basalt compositions.

2. Geological Setting and Samples

The Southwest Indian Ridge (SWIR) is an ultra-slow spreading ridge (∼14 mm/year) extending from the Bouvet Fracture Zone in the west over 7,000 km to the Rodriguez Triple junction in the east (Gao et al., 2016; Patriat & Segoufin, 1988, see Figure 1). The highly oblique spreading center crosses the southern ocean geoid high located over the Marion and Conrad Rise and the Crozet islands (Zhou & Dick, 2013). The Marion Rise extends over 2,200 km with an elevated ridge axis depth of ∼2.0 km. The Marion Rise ranges from 4,800 m water depth at 27°E (Andrew Bain Fracture Zone) to 858 m at 36°E (Prince Edward Fracture Zone), slowly deepening to 5,150 m at the Melville Fracture Zone at 63°E (Gao et al., 2016; Sauter & Cannat, 2010; Zhou & Dick, 2013). Ridge depth and Cr# are positively correlated with Cr# values up to 35, which suggests that the peridotites have experienced approximately 15%–17% of melting of a peridotite (Dick et al., 1984; Hellebrand et al., 2001).

The Andrew Bain Fracture Zone is thought to be a compositional boundary between the sub-ridge mantle in the Atlantic and Indian ocean based on Pb isotope ratios (Dupré & Allègre, 1983), although multi-dimensional isotope data (Sr-Nd-Hf-Pb) do not confirm the difference between MORB from the Atlantic and Indian Ocean (Stracke et al., 2022). The Marion Island hot spot is "noticed" at the ridge through more enriched trace element and isotope signatures between 36°E and 39°E, which is the expected location based on the spreading direction. The top of the Marion Rise is offset to the east of the Marion hotspot, and those basalts do not have isotopic evidence of being influenced by the Marion Hotspot (Mahoney et al., 1992; Zhou & Dick, 2013).

The peridotites investigated in this study (see Figure 1 for locations) were collected during five different cruises to the Southwest Indian Ridge between 25.3°E and 64.5°E. These were the TN365 cruise of the R/V Thompson in 2019 (42°E–45°E), R/V Sonne in 2020 (36.8°E–39.3°E), the Protea cruise of the R/V Melville (MELPROT 5 to SWIR 25°E–46°E; Fisher et al., 1984), and the MD183 (62.5°E–64.5°E; Sauter et al., 2013) and MD 121 cruises (SWIFT, 44°E–44.5°E; Humler, 2001) of the R/V Marion Dufresne (see Figure 1). The peridotites in hand specimens generally have less than 8% modal clinopyroxene (cpx), and most of them are harzburgites (<5% cpx). In addition, most of them are highly serpentinized (50%–90%). Major and trace element concentrations of cpxs and spinels, together with Hf and Nd isotope ratios of the cpxs, are reported in this study.

Basalts reported in this study were collected during two cruises: the TN365 cruise of the R/V Thompson in 2019 (42°E–45°E) and the SO273 cruise of the R/V Sonne in 2020 (36.8°E–39.3°E).

3. Analytical Methods

3.1. Peridotites

The peridotite samples were crushed and sieved; spinel, clinopyroxene, and orthopyroxene separates were handpicked under a binocular microscope and embedded in epoxy for major and trace element analyses. A clinopyroxene fraction was prepared for isotope analyses by pre-concentration using a Frantz Magnetic separator and further handpicking under a binocular microscope.

3.1.1. Major Elements

Major and minor element compositions of orthopyroxene, clinopyroxene and spinel were measured at the Institut für Mineralogie, Universität Münster using a JEOL JXA 8530F electron microprobe analyzer. All elements were calibrated on natural and synthetic, well-characterized mineral and glass reference materials. An accelerating voltage of 15 kV was used throughout the course of this study.

The spinels were analyzed with 40 nA beam current and counting times of 30 s on the peak and 15 s on the background. Silicates (clinopyroxene, orthopyroxene) were measured with a beam current of 15 nA and counting times of 10 and 5 s (peak/bkg) except for Na and K (7s/5s). A set of in-house silicate and spinel standards were measured regularly to check for precision and accuracy. Calibration standards were Jadeite for Na, Olivine San Carlos for Mg, Disthene for Al, Hypersthene for Si, Sanidine for K, Diopside for Ca, Apatite for P, Fayalite for Fe, Rutile for Ti, Ast Cr_2O_3 for Cr, Ast Rhodonite for Mn and NiO for Ni. Detection limits were <300 ppm for Al, <500 ppm for Na, Mg, Si, K, <600 ppm for Ca, Cr, Mn, <700 ppm for P, Fe, <800 ppm for Ni and <1100 ppm for Ti. The phi-rho-z correction was applied to all data and relative uncertainties on major element oxides are on the order of 1%–2%.

3.1.2. Trace Elements

The same sample spots were then ablated for trace element analysis with a spot size of 80 µm, using a 193 nm ArF excimer laser (Analyte G2, Photon Machines) at a repetition rate of 10 Hz and an energy of 3–4 J/cm^2, connected to a Thermo Scientific Element 2 ICP-MS and using NIST-612 glass as the external standard. The latter was analyzed in a block of three different spots between 20 samples. The overall time of a single analysis was 60 s (20 s for background and 40 s for signal integration after switching on the laser). International USGS reference materials BIR-1G, BHVO-2G and BCR-2G were analyzed every 15–20 samples to ensure precision and accuracy over the course of this study (May–November 2021). For the mineral compositions, we present an average of 3–5 individual spots per sample. Summarized major and trace element data of USGS reference materials are given in Table S1. In brief, most trace elements are accurate to within 1%–5% compared to GeoReM preferred values.

3.1.3. Radiogenic Isotope Ratios

Nd-Hf isotope ratios were measured on 100–400 mg of handpicked cpx crystals. Leaching, dissolution, column chemistry and measurements were performed at the National High Magnetic Field Laboratory (NHMFL) at Florida State University using methods described by (Mallick et al., 2014). The separates were leached in ~5 mL 2.5 N HCl and ~500 µL <30% H_2O_2 for 2 hr at room temperature to remove the Mn oxide coating and afterward leached in 6N HCl for around 6 hr at 80°C. The leached separates were rinsed several times with quartz sub-boiling distilled water. Subsequent dissolution and column chemistry were performed after procedures described in Stracke et al. (2003). Nd-Hf isotopes were measured using a Thermo Scientific NEPTUNE Multi-Collector Inductively Coupled Plasma Mass Spectrometer (MC-ICP-MS) at the NHMFL (Mallick et al., 2014). The estimated uncertainties are based on repeated measurements of the La Jolla Nd and JMC-475 Hf standard. The measured value of the La Jolla standard is $^{143}Nd/^{144}Nd = 0.511790 \pm 0.000003$ (2S.E., $n = 28$). The $^{143}Nd/^{144}Nd$ are corrected for mass bias using $^{146}Nd/^{144}Nd$ ratio of 0.7219 and reported relative to La Jolla standard of 0.511850. Blanks for Nd were ~10 pg. The measured $^{176}Hf/^{177}Hf$ are corrected for mass bias using $^{179}Hf/^{177}Hf$ ratio of 0.7325 and reported relative to JMC-475 standard value of $^{176}Hf/^{177}Hf = 0.282160$. Blanks for Hf were <40 pg. The measured average values of the JMC-475 standard are $^{176}Hf/^{177}Hf = 0.282144 \pm 0.000003$ (2S.E., $n = 47$).

For orthopyroxene (sample size between 500–1,500 mg) and cpx isotope analyses of SO273 peridotite samples, the same methodology as described above has been applied at the Institut für Mineralogie, Universität Münster. For samples with modal abundance of cpx <1% and samples size too small to extract enough cpx for isotope analyses, there are orthopyroxene data. Isotope measurements were performed using a Thermo Scientific Neptune *Plus* MC-ICP-MS connected to an Apex Omega desolvating nebulizer system. The $^{143}Nd/^{144}Nd$ values are corrected for mass bias using $^{146}Nd/^{144}Nd$ ratio of 0.7219 and are reported relative to the JNdi standard of 0.512115. The measured $^{176}Hf/^{177}Hf$ are corrected for mass bias using $^{179}Hf/^{177}Hf$ ratio of 0.7325 and reported relative to JMC-475 value of $^{176}Hf/^{177}Hf = 0.282160$. Measured values of the JMC-475 standard are $^{176}Hf/^{177}Hf = 0.282147 \pm 0.000013$ (2 S.E., $n = 17$). As a reference material, USGS BCR-2 was processed as unknown and resulted in $^{143}Nd/^{144}Nd = 0.512642 \pm 0.000014$ (accepted value of GeoReM: 0.512635 ± 0.000029) and $^{176}Hf/^{177}Hf = 0.282869 \pm 0.000006$ (accepted value of GeoReM: 0.282865 ± 0.000013).

3.2. Basalts

For the whole rock analyses, samples were cut with a rock saw and alteration rims were removed. The samples were washed thoroughly in deionized water to remove potential contamination by seawater, coarsely crushed, and ground to powder with an agate mill. The powder was dried for 12 hr at 105°C before being used for further major element and trace element analyses and preparation for Pb-Nd-Hf isotope measurements.

3.2.1. Major Elements

Major element analyses of the whole rock samples were carried out at the GeoZentrum Nordbayern (GZN), Friedrich-Alexander Universität Erlangen-Nürnberg, Germany, with a Spectro XEPOS He X-ray fluorescence spectrometer using fused glass beads following the method described by Woelki et al. (2018). Loss on ignition (LOI) was determined by weighing approximately 1 g of the sample before and after heating the samples for 12 hr at 1300°C. The accuracy and precision of the major elements were determined by multiple measurements of the international rock standards BR and BE-N. The accuracy is generally better than 3.5% except for Na_2O and $P_2O_5$where it is better than 6.4% and 9.4%, respectively. Precision is generally better than 1%, except for Na_2O, which is better than 3.3%.

Eleven lava with fresh glass rinds were crushed and single 1–2 mm sized chips were hand-picked, cleaned in distilled water, embedded in epoxy resin, and polished for electron microprobe and laser ablation ICP-MS analyses. Fresh glasses were analyzed for major and trace element concentrations. Analysis of the major elements (SiO_2, TiO_2, Al_2O_3, FeOt, MnO, CaO, Na_2O, K_2O, P_2O_5 (SO_3 and Cl) was carried out using a JEOL JXA-8200 Superprobe electron probe microanalyzer (EPMA) at the GeoZentrum Nordbayern (GZN), Friedrich-Alexander Universität Erlangen-Nürnberg, Germany. The EPMA was operated with an acceleration voltage of 15 kV, a beam current of 15 nA, and a defocused (10 µm) beam. Counting times were set to 20 and 10 s for peaks and backgrounds for all elements, except for Cl, where peak counting time was 40 s and background times were set to 20 s. Accuracy and precision were determined using the international glass standards VG-2 and VG-A99

measured during each analytical session. For the VG-A99 standard, accuracy is better than 3.7% for all elements except MnO and P_2O_5, and precision is better than 3.3% except for MnO and P_2O_5 (Beier et al., 2018). The average values of 10 spot analyses on each sample and standard are presented in Table S1.

3.2.2. Trace Elements

Trace element analyses basalts were measured at the using a Thermo Scientific X-Series 2 Quadrupole Inductively Coupled Plasma Mass Spectrometer (ICP-MS) connected to an Aridus 2 membrane desolvating sample introduction system at the GeoZentrum Nordbayern (GZN), Friedrich-Alexander Universität Erlangen-Nürnberg, Germany. Standard and sample powders were dissolved using nitric and hydrofluoric acid as reactants (Woelki et al., 2018) Repeated measurements of the international rock standard BHVO-2 yielded an accuracy of better than 4% (2 *S.D.*) for all analyzed elements.

Trace element contents of the glasses were analyzed by laser ablation inductively coupled plasma mass spectrometry (LA-ICPMS) using an Agilent 7900s quadrupole system coupled to a Coherent GeoLas Pro MV 193 nm laser ablation system at the Department of Geosciences and Geography, Environmental and Mineralogical Laboratories (HelLabs) at the University of Helsinki in November 2020. Laser ablation spot sizes of 90 µm in diameter were used with a fluence of 10 J/cm^2 at 10 Hz. The He carrier gas flow was set to 1,050 ml/min. A set of 38 isotopes of 37 elements was measured (^{29}Si, ^{39}K, ^{43}Ca, ^{44}Ca, ^{45}Sc, ^{47}Ti, ^{51}V, ^{52}Cr, ^{60}Ni, ^{63}Cu, ^{66}Zn, ^{71}Ga, ^{85}Rb, ^{88}Sr, ^{89}Y, ^{90}Zr, ^{93}Nb, ^{98}Mo, ^{137}Ba, ^{139}La, ^{140}Ce, ^{141}Pr, ^{146}Nd, ^{147}Sm, ^{153}Eu, ^{157}Gd, ^{159}Tb, ^{163}Dy, ^{165}Ho, ^{166}Er, ^{169}Tm, ^{172}Yb, ^{175}Lu, ^{178}Hf, ^{181}Ta, ^{208}Pb, ^{232}Th and ^{238}U). The dwell time for Si, Ca, Ti, Rb, and Sr was set to 10 and 20 ms for all other elements, a 40-s washout prior and after each analytical period (50 s) was used to ensure sufficient background levels. Analyses of glasses and SRM NIST 612 as secondary reference materials measured as unknown were bracketed by measurements of the SRM NIST610 standard reference material every 15–20 analysis. Oxide formation was monitored by tuning the ThO/Th ratio to ≤0.3% using SRM NIST610, and SRM NIST612 as unknown. Trace element concentrations were internally standardized using Si contents determined by EMPA for the same grain domains. Repeated analysis of SRM NIST612 (n = _6) corrected using SRM NIST610 deviates less than 3% for most elements and 5% for K, Cr, Ba, Pr, Ho, Tm, and ≤8% for Cu and V, respectively, relative to accepted values published in GEOREM for most elements. The long-term accuracy using SRM NIST612 (n = _426) deviates <3% from the published GEOREM values for all isotopes except for Mo, Ba, Pr, Ho, Tm which are <5%, respectively.

3.2.3. Radiogenic Isotope Ratios

Nd-Hf-Pb isotope ratios on basalts were determined as follows: Approximately 90–110 mg of sample powder were leached, dissolved, and processed through ion exchange columns and measured at the National High Magnetic Field Laboratory, Florida State University. The separates were leached in 5 ml 2.5 N HCl and 2 ml 30% H_2O_2 for 60 min at room temperature to remove any alteration products. The leached separates were rinsed several times with quartz sub-boiling distilled water. Subsequent dissolution and column chemistry were performed after procedures described by Stracke et al. (2003). Nd isotope ratios were measured using a Thermo Scientific Neptune MC-ICP-MS. The measured value of the La Jolla Nd standard is ^{143}Nd/^{144}Nd = 0.511799 ± 0.000003 (2*S.D.*, n = 19). The measured ^{143}Nd/^{144}Nd values are corrected for mass bias using a ^{146}Nd/^{144}Nd ratio of 0.7219 and are reported relative to the La Jolla Nd standard of 0.511850. Blanks for Nd were ∼10 pg.

For the digestions and Pb column chemistry double distilled acids were used with dropper bottles to keep the blanks as low as possible. For the separation of Pb, the dissolved samples were loaded on 100 µl Sr-Spec resin columns and washed with 1M HCl. The Pb was collected using 6M HCl. Lead isotope measurements were carried out on a Thermo Scientific Neptune MC-ICP-MS using a ^{207}Pb/^{204}Pb double spike to correct for instrumental mass fractionation at the GeoZentrum Nordbayern (GZN), Friedrich-Alexander Universität Erlangen-Nürnberg, Germany. The double spike, with a ^{207}Pb/^{204}Pb ratio of 0.8135, was calibrated against a solution of the NBS 982 equal atom Pb standard. Samples were diluted with 2% HNO_3 to a concentration of ∼20 ppb, and an aliquot of this solution was spiked to obtain a ^{208}Pb/^{204}Pb ratio of about 1. Spiked and unspiked sample solutions were introduced into the plasma via a Cetac-Aridus desolvating nebulizer and measured in static mode. Interference of ^{204}Hg on mass 204 was corrected by monitoring ^{202}Hg. An iterative exponential mass fractionation correction was applied offline; the correction was typically 4.5 per-mil-per-amu. Twenty measurements of the NBS981 Pb

Table 1
Major Element Composition of Spinels in Abyssal Peridotites From the SWIR

Sample #	Long (E)	Lat. (N)	Axial depth (m)	TiO_2	Al_2O_3	FeO_{tot}	Cr_2O_3	MnO	MgO	NiO	Cr#	Mg#
Protea5D-13-47	25.5367	−53.0950	5300	0.07	50.03	12.79	17.21	0.15	18.29	0.33	18.75	71.82
Protea5D-13-59	25.5367	−53.0950	5300	0.16	29.64	14.17	40.61	0.22	15.08	0.11	47.90	65.48
Protea5D-13-61	25.5367	−53.0950	5300	0.12	48.35	12.14	20.06	0.11	18.58	0.31	21.77	73.17
Protea5D-13-62	25.5367	−53.0950	5300	0.10	48.90	11.59	19.41	0.16	18.67	0.33	21.03	74.17
Protea5D-14-15	25.3267	−53.1133	4150	0.08	52.73	11.41	15.08	0.13	19.63	0.34	16.10	75.41
Protea5D-14-69	25.3267	−53.1133	4150	0.03	45.27	13.04	22.83	0.14	17.79	0.32	25.28	70.86
Protea5D-14-75	25.3267	−53.1133	4150	0.09	46.59	11.84	21.79	0.12	18.63	0.28	23.88	73.73
Protea5D-15-35	32.1467	−47.7000	4400	0.08	51.08	12.38	16.35	0.13	18.81	0.34	17.68	73.05
Protea5D-15-43	32.1467	−47.7000	4400	0.12	47.54	11.99	20.79	0.16	18.34	0.29	22.68	73.18
Protea5D-21-4	35.1567	−45.5150	5040	0.03	36.59	15.24	31.76	0.22	14.89	0.11	36.80	63.53
Protea5D-24-101	35.1767	−45.5750	4400	0.01	45.51	14.81	21.72	0.19	16.34	0.23	24.26	66.30
Protea5D-38-1	46.2883	−39.7150	2800	0.04	48.53	12.10	19.45	0.13	18.62	0.30	21.19	73.29
TN365-D15-1	43.5518	−40.5413	2416	0.12	31.05	14.21	38.09	0.21	15.63	0.16	45.14	66.22
TN365-D15-3	43.5518	−40.5413	2416	0.03	33.02	12.91	37.49	0.21	15.83	0.13	43.24	68.61
TN365-D15-4	43.5518	−40.5413	2416	0.13	32.11	14.01	37.49	0.22	15.65	0.19	43.92	66.57
TN365-D15-5	43.5518	−40.5413	2416	0.10	31.79	14.35	37.32	0.24	15.59	0.17	44.05	65.95
TN365-D18-2	44.4053	−40.2229	1594	0.00	31.81	14.71	37.85	0.25	14.81	0.12	44.39	64.23
TN365-D19-1	44.3682	−40.4773	2911	0.01	26.55	18.00	42.26	0.27	12.72	0.06	51.64	55.74
TN365-D22-5	44.5459	−40.1261	1630	0.10	41.15	12.40	28.10	0.16	17.51	0.20	31.42	71.57
TN365-D22-6	44.5459	−40.1261	1630	0.03	45.92	13.46	21.88	0.18	17.65	0.25	24.22	70.05
TN365-D22-11	44.5459	−40.1261	1630	0.10	38.07	13.32	30.71	0.19	16.95	0.16	35.11	69.42
TN365-D22-23	44.5459	−40.1261	1630	0.08	49.64	11.39	18.88	0.12	18.87	0.29	20.33	74.70
TN365-D22-27	44.5459	−40.1261	1630	0.03	49.38	11.57	19.23	0.15	18.61	0.26	20.71	74.15
TN365-D22-37	44.5459	−40.1261	1630	0.19	31.36	14.43	37.80	0.22	15.82	0.14	44.71	66.15
CON2709-025-138	57.0500	−32.5420	4745	0.05	53.99	11.74	14.19	0.13	19.44	0.38	14.99	74.70
CON2709-006-008	57.1800	−31.9170	3500	0.06	52.40	12.61	15.54	0.12	19.27	0.37	16.59	73.15
SMS_DR01_2_01	62.4802	−28.6830	3512	0.11	54.32	11.01	13.39	0.12	19.90	0.39	14.19	76.32
SMS_DR01_2_02	62.4802	−28.6830	3512	0.06	53.26	11.83	14.18	0.13	19.65	0.32	15.15	74.75
SMS_DR04_2_03	62.4150	−28.9563	3224	0.08	52.81	12.13	14.45	0.12	19.22	0.33	15.51	73.85
SMS_DR06_3_02	62.4833	−28.5253	3238	0.20	42.90	14.10	24.84	0.17	16.99	0.25	27.98	68.24
SMS_DR06_4_06	62.4833	−28.5253	3238	0.13	34.46	15.17	34.13	0.20	15.46	0.16	39.92	64.50
SMS_DR06_4_14	62.4833	−28.5253	3238	0.12	40.72	13.38	27.58	0.19	16.97	0.22	31.24	69.35
SMS_DR08_2_08	62.5902	−28.5152	4370	0.51	38.55	19.24	24.97	0.20	15.52	0.28	30.29	58.98
SMS_DR10_5_06	62.4685	−28.5592	3602	0.12	53.52	11.62	14.32	0.10	19.60	0.34	15.22	75.05
SMS_DR11_2_06	62.5588	−28.0620	3145	0.25	46.84	13.55	20.59	0.19	17.81	0.26	22.77	70.10
SMS_DR11_2_11	62.5588	−28.0620	3145	0.11	45.28	13.17	22.53	0.17	17.69	0.24	25.03	70.54
SMS_DR11_2_13	62.5588	−28.0620	3145	0.08	46.79	12.97	21.25	0.17	17.98	0.22	23.35	71.20
SMS_DR26_2_12	64.6465	−28.1497	3712	0.08	44.01	11.95	24.91	0.15	18.17	0.24	27.52	73.05
SMS_DR27_2_09	64.5305	−27.8102	2570	0.31	44.77	15.51	21.34	0.18	17.16	0.26	24.23	66.36
SMS_DR27_3_28	64.5305	−27.8102	2570	0.15	31.34	16.05	36.49	0.21	15.35	0.17	43.85	63.04
SMS_DR29_5_02	64.5548	−27.8180	2604	0.10	53.95	12.15	13.01	0.12	19.46	0.33	13.93	74.06
SC08-10	45.5100	−39.5000		0.11	49.85	12.67	17.87	0.16	17.86	0.25	19.39	71.55
SC08-05	45.5100	−39.5000		0.13	44.21	13.91	23.96	0.19	16.44	0.19	26.66	67.81

Table 1
Continued

Sample #	Long (E)	Lat. (N)	Axial depth (m)	TiO_2	Al_2O_3	FeO_{tot}	Cr_2O_3	MnO	MgO	NiO	Cr#	Mg#
SWIFT_DR26_2_04	44.0337	−40.9770	3070	0.04	50.61	12.04	16.82	0.13	19.24	0.33	18.23	74.02
SWIFT_DR26_3_04	44.0337	−40.9770	3070	0.07	22.80	20.28	42.60	0.28	13.14	0.18	55.62	53.60
SWIFT_DR26_2_03	44.0337	−40.9770	3070	0.06	55.97	12.02	11.01	0.14	19.51	0.41	11.66	74.31
SO273-DR6-30	44.435	37.147	2427	0.03	39.33	14.54	29.28	0.18	15.79	0.17	33.32	65.93
SO273-DR6-37	44.435	37.147	2427	0.05	38.05	15.43	29.89	0.20	15.55	0.17	34.52	64.24
SO273-DR6-41	44.435	37.147	2427	0.04	37.07	14.84	31.53	0.20	15.24	0.13	36.34	64.68
SO273-DR6-53	44.435	37.147	2427	0.04	36.69	14.73	32.03	0.20	15.51	0.15	36.94	65.25
SO273-DR6-62	44.435	37.147	2427	0.07	36.12	14.22	32.41	0.18	15.76	0.17	37.58	66.39
SO273-DR1-1	44.827	36.900	2221	0.03	29.02	19.02	38.48	0.27	12.40	0.11	47.08	53.75
SO273-DR19-1	44.547	38.161	2468	0.03	47.85	16.08	18.01	0.16	16.44	0.26	20.16	64.57

isotope standard (measured as an unknown) throughout this study gave $^{206}Pb/^{204}Pb$, $^{207}Pb/^{204}Pb$, $^{208}Pb/^{204}Pb$ of 16.9459, 15.5019, and 36.7301, respectively. The Pb blanks are less than 30 pg.

4. Results

4.1. Peridotites

Major element data for the spinels are reported in Table 1. Major-trace element contents and isotope ratios for clinopyroxenes and orthopyroxenes from the peridotites are listed in Table S2. The spinels from the peridotites fall within the range of abyssal peridotites on a Mg# versus Cr# diagram (Figure 2) and range to high Mg# (76) with low Cr# (14) to Mg# = 53 with Cr# = 55, which is at the depleted range for abyssal peridotites. The spinel in these peridotites have distinctly lower Cr# than those of subduction related peridotites such as those from Izu-Bonin (61 ± 11; Zanetti et al., 2006) or the Tonga arc (Birner et al., 2017; Zanetti et al., 2006). Most of the analyzed peridotites have TiO_2 concentrations in spinel <0.15 wt. %. The TiO_2 contents in the spinels correlate positively with the Yb contents of the cpx (Figure S1 in Supporting Information S1). In general, the peridotites have a residual character, that is, their cpx are light REE depleted (see Figure 3), except for samples TN365 D18-2 and TN365 D19-1 (black patterns in Figure 3b) and SMS DR27-3-28 samples (hatched black patterns in Figure 3c).

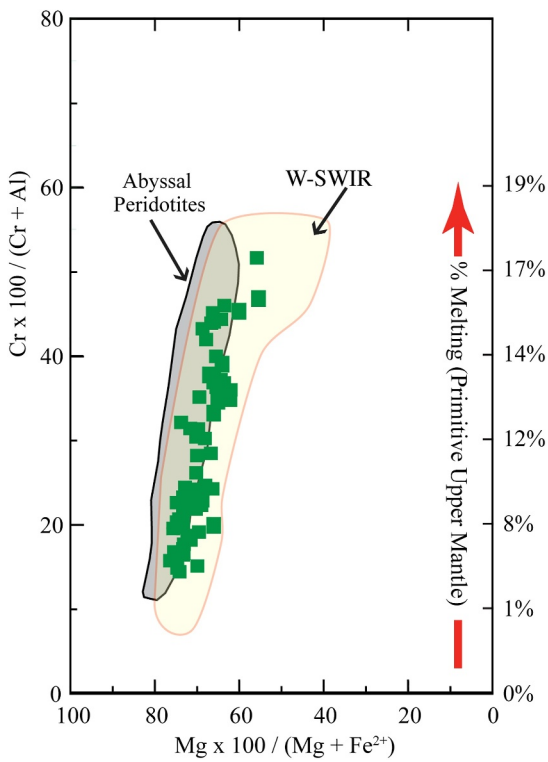

Figure 2. Cr# versus Mg # for abyssal peridotites east of the Andrew Bain Fracture Zone. Also shown is the field from SWIR west of the Fracture zone. Data from (Johnson et al., 1990; Mallick et al., 2014; Salters & Dick, 2002; Standish et al., 2002). Right hand axis indicates the degree of depletion relative to bulk silicate Earth from Hellebrand et al. (2001).

We have five Hf–Nd isotope data on orthopyroxenes from samples with very low modal abundance of cpx, that is, harzburgites with less than 1% modal cpx. It is assumed that, like cpx, the orthopyroxene isotope ratio represents the whole rock composition. This is supported by the measurement of one cpx-opx pair whose Hf-Nd isotope ratios are within error of each other. Overall, five peridotites have cpx and an additional three have opx with unradiogenic Nd ($\varepsilon_{Nd} < 0$). The opx data were obtained on harzburgites with less than 1% modal cpx and, except for one sample, the cpx content was too low for isotopic analysis. The isotopic compositions of the one cpx-opx pair agree with each other within error.

The combined cpx -opx of the SWIR peridotites range from ε_{Hf} of −19 to 417 and ε_{Nd} of −18 to 93 (Figure 4a), thus mostly falling above the terrestrial MORB-OIB $\varepsilon_{Hf} - \varepsilon_{Nd}$ trend (Jones et al., 2019; Vervoort & Blichert-Toft, 1999). The Hf-Nd isotope ratios are not correlated with major or trace element concentrations, but the isotopic variability generally increases with lower Yb and Al_2O_3 contents of the cpx and decreasing TiO_2 content in spinel (Figure 5).

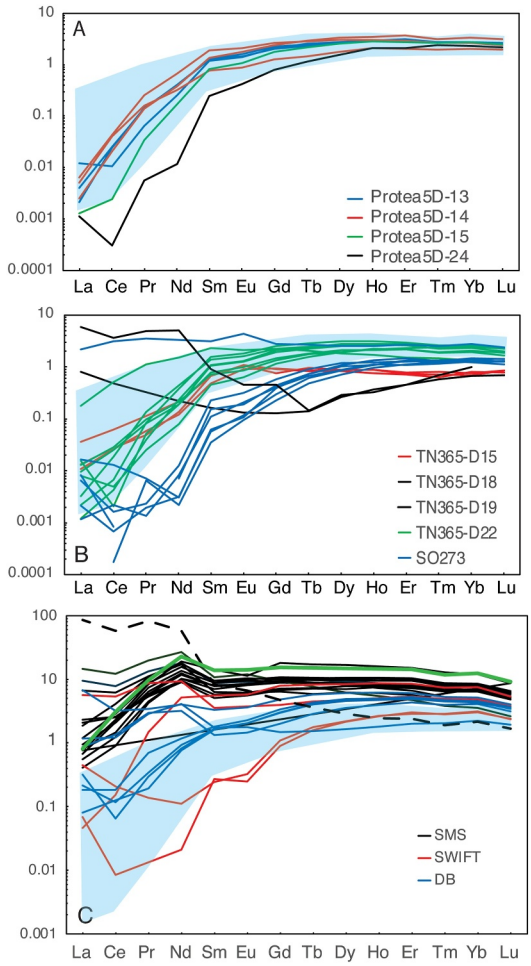

Figure 3. REE patterns of cpx from three separate areas: panel (a). Protea (53°E−38°E), panel (b) TN365 (43.5°–44.5°E) and panel (c) SMS (62.4°E−64.6°E). REE patterns are normalized to the bulk silicate Earth (McDonough & Sun, 1995). Two black lines in (b) and a hatched black line in (c) are the cpxs mentioned in the text. The blue field in the background encompasses the LREE depleted cpx from the 52° to 63°E of Seyler et al. (2011).

4.2. Basalts

Table 2 reports the basalt Nd, Hf and Pb isotope ratios. The major element contents of the basalts overlap with those of previous studies of MORB from the SWIR (compiled from PetDB) and have MgO contents between 9.0 and 6.5 wt. %. Westward along the shallowing Marion Rise, the running average of $Na_{8.0}$ decreases from 3.8 to 2.5 (Figure S2 in Supporting Information S1). There is an abrupt change in the MORB chemistry west of the Andrew Bain Fracture Zone where Na_8 becomes distinctly higher (average of 3.1) and Ti_8 increases as well (average of 1.4–1.6) excluding anomalous basalts from the Du Toit Fracture Zone (Janney et al., 2005).

Basalts have flat to light REE-enriched patterns. Almost all of the basalts have $(La/Sm)_N > 1.5$ and can be classified as E-MORB (Gale et al., 2013). Notably, basalts from two dredges at the near-ridge Mahoney seamount close to the Eric Simpson fracture zone are highly incompatible element-enriched (Woelki et al., 2023). The range of Hf and Nd isotope ratios of the basalts analyzed in this study is large; ε_{Hf} ranges from −1.0 to 33.0 and ε_{Nd} from −8 to 11. There are several basalts that fall well outside the field for global MORB toward higher Hf isotope ratios (Figure 4b). The vertical deviation in Hf isotopes from the MORB–OIB regression line (Chauvel et al., 2008; Jones et al., 2019; Vervoort et al., 2011) can be quantified by the parameter $\Delta\varepsilon_{Hf}$ (see also (Pearce et al., 1999). The largest $\Delta\varepsilon_{Hf}$ we observe is +25, and five basalts have $\Delta\varepsilon_{Hf}$ values higher than 10. Although $\Delta\varepsilon_{Hf}$ of 10 is an arbitrary distinction, it is clear that these basalts are outliers from the main correlated field and lie distinctly above the global MORB-OIB Hf-Nd isotope trend.

Dredge 30 of expedition TN365 at 38.87°E recovered highly vesicular basalts from 1000 m depth on top of the Marion Rise. These basalts have significantly higher Na_2O contents with Na_8 close to 4. They also have high incompatible element contents with Nb > 15ppm, La/Sm up to 4 and Sr up to 700ppm. These basalts have ε_{Nd} between 0.0 and 1.5 and ε_{Hf} between 3.3 and 4.0 and are clearly derived from a source, on average, more incompatible element enriched than MORB.

5. Discussion

The large Nd-Hf isotopic difference between the basalts and the cpxs from the nearby abyssal peridotites of the SWIR is striking (Figure 4a). The Hf-isotope ratios of most of the peridotite cpx are well outside the range of any MORB, which has also been recognized in several locations along the global mid-ocean ridge system (Cipriani et al., 2004; Salters, 2025; Salters & Dick, 2002; Sani et al., 2004, 2023; Stracke et al., 2011). Moreover, Johnson et al. (1990) showed that the cpx trace element concentrations of most peridotites are not in equilibrium with MORB-like magmas. Our data also shows that the REE patterns of peridotite cpx at the Marion Rise are not in equilibrium with the spatially associated MORB (Figure S3 in Supporting Information S1), which underscores the isotopic differences. That is, this data precludes a simple melt-residue relation between the basalts and associated peridotites.

The isotopic differences between the peridotite cpx and the spatially associated MORB require that, in addition to the peridotites, there must be incompatible element enriched component with lower Hf and Nd isotope ratios that contribute a significant fraction of incompatible elements to the aggregated melts, that is, the sampled MORB (Brunelli et al., 2018; Mallick et al., 2014; Salters & Dick, 2002; Stracke et al., 2011). The occurrence of highly incompatible element enriched MORB along the SWIR (Seyler et al., 2011; Zhang et al., 2024), and the incompatible element enriched basalts from dredge TN365-D30 as well as the low Nd-isotopic compositions of peridotites from expedition SO273 show that incompatible element enriched component(s) with low Hf-Nd isotope ratios must indeed be present in the mantle under the SWIR.

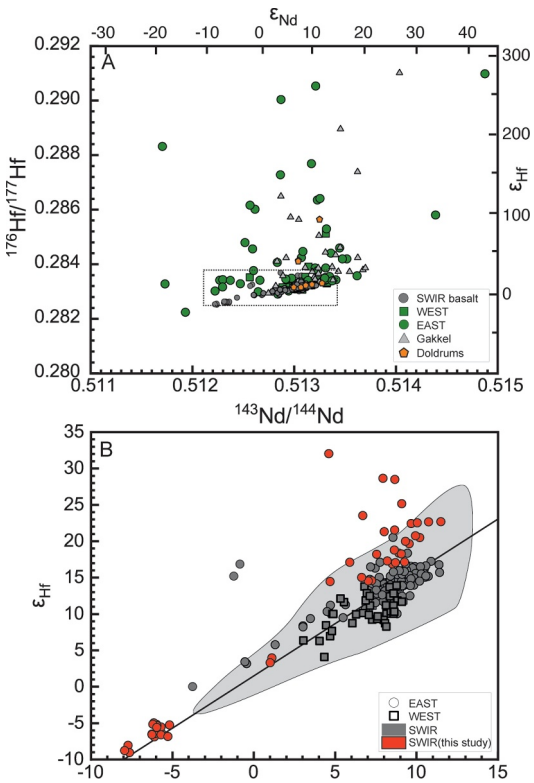

Figure 4. (a). Hf-and Nd isotopic composition of cpxs from abyssal peridotites from the SWIR east of Andrew Bain Fracture Zone (dark blue squares), west of Andrew Bain Fracture Zone (light blue diamonds), Gakkel (red circles) and Doldrums. The most extreme isotopic composition of $\varepsilon_{Nd} = 97$ and $\varepsilon_{Hf} = 417$ is not shown to better view the data. Data from this study and (Mallick et al., 2014, 2015; Salters & Dick, 2002, 2011; Sani et al., 2020; Stracke & Snow, 2009). Gakkel data from (Salters, 2025). (b). Basalt Hf and Nd isotope data show both the large range in isotopic composition of the basalts as well as the deviation of some of the basalts to higher Hf-isotopic compositions. Pacific, Atlantic and Indian Ocean data are compilations from EarthChem/PetDb. Published data for the SWIR are from (Janney et al., 2005; Mallick et al., 2015; Meyzen et al., 2005, 2007; Paquet et al., 2020; Wang et al., 2020).

Below we will provide a model for the formation of high Hf-ratio peridotites and the decoupling of the Nd and Hf isotope systems. As both the Hf and Nd isotopic compositions are more radiogenic than bulk silicate Earth, melt depletion must have played an important role in the origin of the isotopic compositions. In addition, we will explore the constraints provided by the major and trace elements of the cpx and spinel on the individual stages of the history of the peridotites.

5.1. Abyssal Peridotite Evolution

5.1.1. Peridotite Evolution by Repeated Cycles of Partial Melting and Melt-Rock Reaction

The parent-daughter variations through time are affected by melt depletion and enrichment. Based on trace element partitioning experiments (Salters et al., 2002; Salters & Longhi, 1999) in fertile peridotites cpx and garnet are the two main mineral phases that host the REE and Hf. As peridotites melt incongruently the garnet and cpx contribution to the melt is higher than other mineral phases (Longhi, 2002) and therefore at higher degrees of depletion orthopyroxene will contain a significant amount of the REE budget of a peridotite, albeit in a peridotite with far lower whole-rock concentrations. Thus, the peridotite parent-daughter variations through time are mainly controlled by garnet and cpx partitioning.

The high Hf isotope ratios of the SWIR peridotites, well above the terrestrial Hf–Nd array (Chauvel et al., 2008; Jones et al., 2019; Vervoort & Blichert-Toft, 1999), are the result of a high Lu/Hf produced during melting several 100–1,000 million years ago. However, this ancient melting would also have resulted in high Sm/Nd and consequently high Nd isotope ratios, much higher than those in MORB and higher than what is observed in most of the abyssal peridotites, including those from the SWIR. An ε_{Hf} value of 400, for example, can develop in a peridotite that has melted to ~10% 1 Ga ago, but this would also lead to ε_{Nd} ~200. Although, abyssal peridotites do show Nd-isotope ratios that are distinctly higher than MORB values (Cipriani et al., 2004; Mallick et al., 2015; Salters & Dick, 2002; Stracke et al., 2011), the Nd-isotope ratio deviation is small compared to the Hf-isotope ratios and the time-integrated Sm/Nd fractionation therefore has to be, in a relative sense, much less than that for Lu/Hf. The decoupling between Hf and Nd isotope ratios therefore requires a more complex, multi-stage (Stracke et al., 2011). The lower Nd isotope ratios for high Hf isotope ratios observed in many peridotites from the SWIR therefore require an addition of or reaction with an infiltrating melt to either lower the Sm/Nd ratio in the past or lower the $^{143}Nd/^{144}Nd$ more recently (Sanfilippo et al., 2019, 2024; Sani et al., 2023; Stracke et al., 2011), while the high $^{176}Hf/^{177}Hf$ signature is not completely eradicated.

Nd is slightly more incompatible than Hf during peridotite melting and is therefore, in a relative sense, depleted to a larger extent than Hf, and the Nd/Hf ratio of the residue thus decreases as a result of partial melting, and for most melting scenarios so does the (Lu/Hf)/(Sm/Nd) (Salters et al., 2002; Salters & Longhi, 1999). Conversely, a melt has relatively lower Sm/Nd compared to Lu/Hf, but higher Nd/Hf. Hence, during reaction of a high-Nd/Hf-melt with a low-Nd/Hf-melt-depleted-peridotite, the $^{143}Nd/^{144}Nd$ and the Sm/Nd in the reacted peridotite are changed more effectively toward the melt composition than the $^{176}Hf/^{177}Hf$ and Lu/Hf (Sanfilippo et al., 2019; Stracke et al., 2011).

This model of initial depletion followed by melt addition is shown in Figure 6. Each model curves in Figure 6 represents melting of an average depleted mantle (DM, Salters & Stracke, 2004), to different degree (2%–16%) followed by melt addition. The different curves represent different ages of the melting event ranging from 0.5 Ga to 3 Ga. The melt addition, in all cases, is assumed to be an E-MORB-like composition. The purpose of these model calculations is to show that such a two-stage evolution can explain the decoupling of the Hf from the Nd

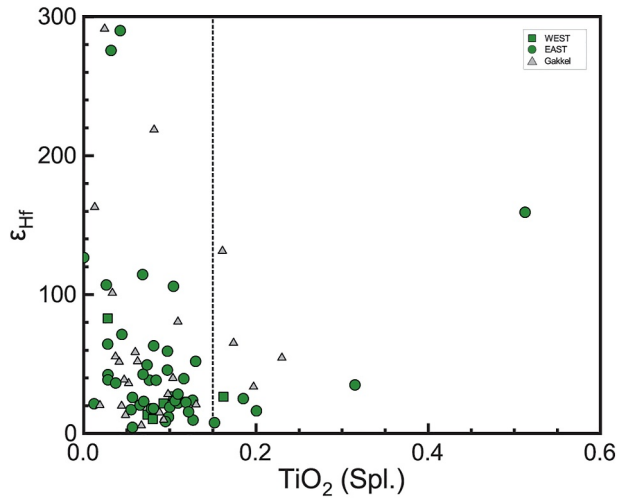

Figure 5. TiO_2 in spinel versus Hf-isotopic composition. TiO_2 values of less than 0.15 wt% (hatched line) is taken as evidence for a pure residual character. Data from SWIR This study and (Mallick et al., 2014) as well as Gakkel Ridge from Stracke & Bourdon (2009) as well as (Salters, 2025).

isotope ratios. But abyssal peridotites sampled today have also melted during recent ascent beneath the ridge. Thus, abyssal peridotites have undergone at least a three-stage process: ancient and recent melting, and melt-rock reaction, either in the past or during recent ascent under the ridge, or both.

The REE patterns for evolution models with 6%, 10%, and 15% of initial melting are shown in Figures 6b–6d, respectively. The cpx composition after stage 1 (ancient melting), stage 2 (melt addition) and stage 3 (recent melting) are shown as well as the field of the Marion Rise abyssal peridotite cpx which overlaps with the stage 3 cpx composition. However, there are few constraints on the model other than the requirement of a melt depletion and subsequent addition of a melt.

Whether the timing of the melt reaction is recent or ancient cannot be determined unambiguously by the isotopic composition alone (see also (Sani et al., 2024; Stracke et al., 2011). This is seen in Figure 6. The 3 Ga evolution curve that is calculated for both re-enrichment with E-MORB immediately after melt depletion at 3 Ga and recent enrichment just prior to or during ascent beneath the ridge. Both scenarios lead to extreme Hf-isotopic composition and decoupling of the Hf-Nd systematics. But the combined trace element concentrations and Hf-Nd isotope ratios can further constrain the timing of the melt-rock reaction (Sani et al., 2023), which is discussed next.

5.1.2. Timing of Melt-Peridotite Reaction

The REE patterns of the cpx reflect only the final integrated stage of a multi-stage evolution. Notably, the order of the events determines the REE patterns, but they are independent of the timing of the individual events. The REE patterns of three scenarios with initial melt depletion of 6%, 10% and 16% are shown in Figure 6. In all three scenarios, the peridotites experience 0.5% addition of a melt with E-MORB characteristics immediately after the ancient melt depletion and 6% melt extraction during recent ascent. The difference between the recent enrichment and enrichment immediately following depletion is shown in Figure 6a for a 3 Ga depletion event. For the same melt composition, recent melt addition has a somewhat smaller effect on the Nd-Hf ratios than ancient enrichment. This example shows that the timing of the melt peridotite reaction is not well constrained as there are multiple scenarios that can explain the isotopic compositions, especially considering that the composition of the melt added is not well known.

The E-MORB used in our model is just an arbitrary choice. A LREE-enriched melt will affect the Sm/Nd ratio more than the Lu/Hf ratio. It should be noted that only a small addition of melt is needed to decouple the Nd from the Hf system as long as this melt has an elevated Nd/Hf ratio relative to the peridotites. The calculations also show that many combinations of depletion followed by enrichment can decouple Lu/Hf from Sm/Nd. Nevertheless, there are several conclusions that can be drawn from these calculations. First, the depletion event that results in the Lu/Hf and subsequently radiogenic $^{176}Hf/^{177}Hf$ has to be ancient (>1 Ga, see Figure 6) to produce $^{176}Hf/^{177}Hf$ far higher than those in MORB. Second, with an initial peridotite composition similar to the depleted mantle (Salters & Stracke, 2004), at least 6% of melt must have been extracted in the past to yield the high Hf-isotope ratios. Third, the high Lu/Hf and high Sm/Nd resulting from the ancient depletion event can be altered effectively by less than 1% addition of an enriched melt, such as E-MORB, resulting in drastic changes of the Sm/Nd and Lu/Hf of the reacted peridotite.

5.1.3. Compositional Constraints on Multi-Stage Peridotite Evolution

The major and trace element systematics of the peridotite mineral compositions can further constrain the enrichment and depletion events and the order in which they have occurred. The Cr# in spinel ranges from 12 to 54 (see Figure 2), which indicates a total of ~2%–17% melt depletion of the SWIR peridotites when approximated as a simple one stage depletion assuming a bulk silicate Earth initial composition (Hellebrand et al., 2001).

Geochemistry, Geophysics, Geosystems

10.1029/2025GC012418

Table 2
Basalt Isotopic Compositions

Sample #	IGSN sample #	Long [E]	Lat. [N]	Axial depth [m]	$^{206}Pb/^{204}Pb$	$^{207}Pb/^{204}Pb$	$^{208}Pb/^{204}Pb$	$^{143}Nd/^{144}Nd$	2 sigma error	ε_{Nd}	$^{176}Hf/^{177}Hf$	2 sigma error	ε_{Hf}	$\Delta\varepsilon_{Nf}$
SO273-ROV451-6	GFSO273AA6	37.0910	−44.5600	2591	18.251	15.510	38.006	0.513094	±10	9.06	0.283301	±7	18.26	3.56
SO273-ROV451-8	GFSO273AA8	37.0910	−44.5600	2591				0.513038	±5	7.95	0.283388	±12	21.31	8.21
SO273-D11-1	GFSO273C22	37.1380	−44.5230	2722	18.591	15.676	38.714	0.513001	±4	7.24	0.283198	±5	14.59	2.51
SO273-D11-4	GFSO273C25	37.1380	−44.5230	2722				0.512901	±11	5.30				
SO273-D11-6	GFSO273C27	37.1380	−44.5230	2722	18.487	15.537	38.261	0.512995	±5	7.11	0.283162	±6	13.33	1.43
SO273-D12-10	GFSO273D31	37.1670	−44.5040	2174	18.520	15.539	38.274	0.512969	±5	6.62	0.283210	±5	15.03	3.84
SO273-D12-7	GFSO273D28	37.1670	−44.5040	2174				0.512973	±5	6.69	0.283451	±12	23.54	12.24
SO273-D12-9	GFSO273D30	37.1670	−44.5040	2174	18.541	15.553	38.314	0.512990	±4	7.03	0.283196	±4	14.55	2.77
SO273-D14-5	GFSO273E26	38.0200	−44.2980	2340				0.513017	±8	7.54	0.283300	±15	18.22	5.69
SO273-D15-10	GFSO273F31	38.2520	−44.2670	2573				0.513096	±11	9.08	0.283496	±7	25.16	10.42
SO273-DR16-20	GFSO273G41	38.2820	−44.2220	2545				0.513026	±3	7.72	0.283204	±8	14.81	2.02
SO273-DR16-26	GFSO273G47	38.2820	−44.2220	2545	17.960	15.545	37.811	0.513082	±5	8.82	0.283217	±5	15.29	0.92
SO273-DR16-9	GFSO273G30	38.2820	−44.2220	2545	17.550	15.482	37.486	0.512870	±5	4.68	0.283194	±5	14.48	6.07
SO273-DR30-1	GFSO273M22	38.8700	−43.8850	1054	16.789	15.434	37.287	0.512238	±4	−7.64	0.282530	±4	−9.03	0.32
SO273-DR30-11	GFSO273M32	38.8700	−43.8850	1054	16.880	15.466	37.321	0.512318	±7	−6.09	0.282603	±13	−6.45	0.66
SO273-DR30-14	GFSO273M35	38.8700	−43.8850	1054	16.902	15.465	37.326	0.512309	±5	−6.26	0.282599	±5	−6.57	0.78
SO273-DR30-20	GFSO273M41	38.8700	−43.8850	1054	16.899	15.467	37.340	0.512338	±5	−5.70	0.282599	±5	−6.58	−0.03
SO273-DR30-26	GFSO273M47	38.8700	−43.8850	1054	16.800	15.474	37.332	0.512220	±4	−8.00	0.282538	±5	−8.74	1.11
SO273-DR30-29	GFSO273M50	38.8700	−43.8850	1054	17.012	15.475	37.444	0.512361	±5	−5.24	0.282637	±6	−5.23	0.65
SO273-DR30-3	GFSO273M24	38.8700	−43.8850	1054				0.512237	±2	−7.67	0.282557	±3	−8.05	1.34
SO273-DR30-4	GFSO273M25	38.8700	−43.8850	1054	16.889	15.470	37.336	0.512356	±4	−5.34	0.282593	±4	−6.81	−0.78
SO273-DR30-7	GFSO273M28	38.8700	−43.8850	1054	16.885	15.470	37.334	0.512317	±6	−6.11	0.282591	±6	−6.87	0.27
SO273-DR30-8	GFSO273M29	38.8700	−43.8850	1054	16.882	15.466	37.324	0.512309	±4	−6.26	0.282602	±5	−6.49	0.87
SO273-DR30-9	GFSO273M30	38.8700	−43.8850	1054	16.883	15.468	37.328	0.512340	±6	−5.66	0.282604	±5	−6.42	0.07
SO273-DR31-1	GFSO273N22	38.8800	−43.8540	728	16.921	15.473	37.385	0.512324	±3	−5.98	0.282639	±5	−5.16	1.79
SO273-DR31-13	GFSO273N34	38.8800	−43.8540	728	16.916	15.472	37.385	0.512315	±5	−6.14	0.282645	±7	−4.95	2.24
SO273-DR31-16	GFSO273N37	38.8800	−43.8540	728	17.094	15.504	37.549	0.512325	±7	−5.96	0.282635	±7	−5.31	1.61
SO273-DR31-18	GFSO273N39	38.8800	−43.8540	728	16.995	15.480	37.441	0.512312	±11	−6.20	0.282640	±8	−5.13	2.13
SO273-DR31-3	GFSO273N24	38.8800	−43.8540	728	16.912	15.471	37.378	0.512338	±4	−5.70	0.282629	±5	−5.52	1.04
SO273-DR31-8	GFSO273N29	38.8800	−43.8540	728	16.940	15.471	37.394	0.512321	±5	−6.02	0.282628	±5	−5.56	1.44
TN365-D6-1		43.2169	−40.5437		18.235	15.522	38.089	0.513122	±4	9.60	0.283341	±4	19.67	4.19
TN365-D6-2		43.2169	−40.5437					0.513125	±5	9.66	0.283420	±4	22.45	6.87
TN365-D5-1		43.2394	−40.5032					0.513177	±8	10.68	0.283426	±4	22.66	5.62
TN365-D5-7		43.2394	−40.5032		17.794	15.481	37.664	0.513153	±4	10.19	0.283365	±4	20.51	4.17

Geochemistry, Geophysics, Geosystems

10.1029/2025GC012418

Table 2
Continued

Sample #	IGSN sample #	Long [E]	Lat. [N]	Axial depth [m]	$^{206}Pb/^{204}Pb$	$^{207}Pb/^{204}Pb$	$^{208}Pb/^{204}Pb$	$^{143}Nd/^{144}Nd$	2 sigma error	ε_{Nd}	$^{176}Hf/^{177}Hf$	2 sigma error	ε_{Hf}	$\Delta\varepsilon_{Nf}$
TN365-D7-11		43.2617	−41.0081					0.513142	±9	9.99	0.283423	±6	22.55	6.50
TN365-D7-26		43.2617	−41.0081					0.513216	±6	11.43	0.283427	±5	22.71	4.59
TN365-D10-34		43.4116	−40.5822		17.902	15.476	37.831	0.513087	±4	8.91	0.283304	±4	18.37	3.87
TN365-D10-56		43.4116	−40.5822		17.847	15.469	37.739	0.513139	±4	9.93	0.283372	±5	20.77	4.81
TN365-D27-1		44.5948	−40.2570					0.512932	±11	5.89	0.283269	±8	17.13	6.99
TN365-D27-10		44.5948	−40.2570		18.021	15.492	37.930	0.513078	±5	8.73				
TN365-D27-12		44.5948	−40.2570					0.513071	±5	8.60	0.283394	±4	21.55	7.52
TN365-D27-3		44.5948	−40.2570		18.024	15.509	38.009	0.513040	±5	8.00	0.283596	±15	28.66	15.48
TN365-D27-32		44.5948	−40.2570		17.962	15.478	37.949	0.513067	±5	8.52	0.283263	±6	16.90	2.98
TN365-D27-33		44.5948	−40.2570		17.973	15.490	37.977	0.512951	±9	6.26	0.283691	±24	32.05	21.38
TN365-D27-38		44.5948	−40.2570		17.963	15.480	37.954	0.513078	±3	8.75	0.283268	±7	17.07	2.81
TN365-D27-4		44.5948	−40.2570		17.964	15.481	37.955	0.513105	±3	9.26	0.283270	±4	17.15	2.16
TN365-D27-41		44.5948	−40.2570		17.878	15.370	37.588	0.513071	±15	8.60	0.283591	±3	28.50	14.45
TN365-D27-45		44.5948	−40.2570		17.963	15.480	37.955	0.513053	±3	8.26	0.283274	±5	17.29	3.75
TN365-D27-5		44.5948	−40.2570		18.035	15.501	37.953	0.513072	±10	8.63	0.283317	±5	18.81	4.72
TN365-D27-7		44.5948	−40.2570		18.025	15.496	37.940	0.513026	±8	7.73				
TN365-D30-1		45.2795	−40.0884					0.512667	±4	0.71				
TN365-D30-2		45.2795	−40.0884					0.512681	±3	1.00	0.282879	±6	3.31	0.21
TN365-D30-4		45.2795	−40.0884					0.512689	±4	1.16	0.282898	±7	3.98	0.65
TN365-D30-6		45.2795	−40.0884					0.512706	±4	1.48				
TN365-D30-9		45.2795	−40.0884					0.512631	±6	0.03				

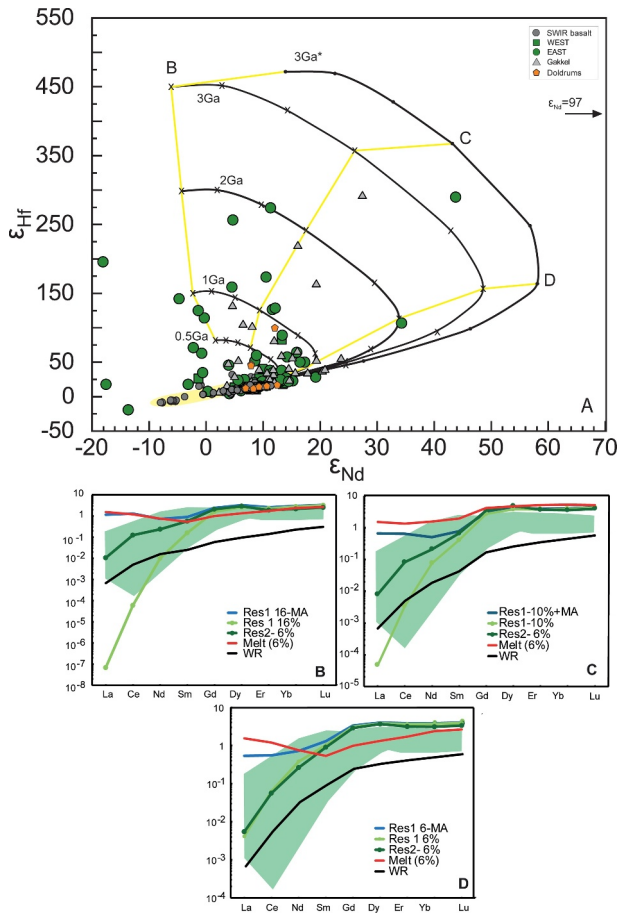

Figure 6. (a) Hf-Nd isotope space where curves represent the present day isotopic composition of peridotites with DM composition that have been depleted by melting followed by the addition of an E-MORB type melt. Each curve represents the age (0.5 Ga, 1.0 Ga, 2.0 Ga and 3.0 Ga) at which the initial melt depletion occurred. Symbols on curves represent 2%, 4%, 6%, 8%, 10%, 12%, 14%, and 16% melt depletion and the melting model follows Salters et al. (2002). For all scenarios, the first 4% of melt is extracted in the garnet stability field. The melt reaction by E-MORB addition of 0.5% is immediately after the initial extraction. The 3.0 Ga* curve with solid circles as symbols is for a 3 Ga melting event and present-day addition of 0.5% E-MORB instead of addition immediately after melting. The yellow lines connect the cpx with the same events and only difference in timing. The extent of the initial melt depletion determines the effect of melt addition or reaction on the Sm/Nd and the timing of both events determines how different the $^{143}Nd/^{144}Nd$ will develop from MORB-like values. Black squares represent SWIR, blue circles represent Gakkel, and green triangles represent Doldrums FZ cpxs. Data from this study as well as (Mallick et al., 2015; Salters & Dick, 2011; Sani et al., 2023; Stracke et al., 2011; Stracke & Snow, 2009). Field for MORB field in yellow from PetDb. Panels (b–d) show the normalized REE patterns of the cpx in peridotites at different stages of evolution. The different panels are for different degrees of initial depletion: 16% (a), 10% (b) and 6% melt (c). Cpx in residue after initial depletion is labeled as Res 1 (light green), followed by cpx after melt addition (MA, blue) and cpx pattern after recent melting of 6% with dark green patterns (Res2) and the derived melt composition in red, and residual bulk solid in black in all there inset diagrams. The green shaded field in the diagram is the range of REE depleted cpx compositions of the Marion Rise abyssal peridotites. The observed compositions of the cpx in the peridotites overlapped with the modeled compositions.

Except for three samples, the REE patterns of the cpx from the Marion Rise peridotites are light REE depleted (Figure 3). Melt enrichment is also noticed by enrichment of La with respect to Ce and deviation from a smooth REE pattern. Apart from the LREE enriched samples there are three samples with LREE depleted patterns but with slightly elevated La content, which indicate potentially minor melt addition, or simply seawater alteration with high La/Ce. In addition. The Ce/Yb ratios in the cpxs are not correlated with other chemical parameters, indicating the possibility of small amounts of melt infiltration. The HREE abundances in the cpx decrease with increasing Cr# in the spinel and/or cpx (see Figure S1 in Supporting Information S1) and HREEs (Gd-Lu) are generally well correlated, indicating control by melt depletion (Brunelli et al., 2014; Warren & Shimizu, 2010).

The melt depleted character is confirmed by the uniformly low TiO_2 content of the spinels (see Figure 5). Therefore, the peridotites investigated here did not have a significant interaction with melt subsequent to or contemporaneous with partial melting during their recent ascent under the SWIR. This is not to say that a melt reaction did not occur during the Marion Rise peridotite evolution. Melt depletion leads to correlated Ti-Zr and Ce-Yb variations, while deviation from this trend to higher Zr (Ce) for a given Ti (Yb) indicates a reaction with migrating or stalled melts (Brunelli et al., 2006; Mallick et al., 2014). The latter is often observed for peridotites from the SWIR investigated in previous studies (Brunelli et al., 2014; Seyler et al., 2003, 2007; Warren & Shimizu, 2010; Figure 7). The cpx analyzed in this study fall along and to the right of the depletion trends in Figure 7, indicating that some, but not all, have experienced some form of melt-rock reaction. Therefore, despite low TiO_2 in spinel and light REE depleted patterns, there is evidence for a melt-rock reaction as indicated by slightly elevated Zr relative to Ti contents (Figure 7). However, based on the REE patterns and the low TiO_2 content, this melt reaction must have been followed by melting that is, the reaction of the peridotites with a melt occurred before recent remelting under the SWIR.

The REE patterns show general similarities with the patterns for the LREE depleted cpx from peridotites sampled at the SWIR between 52°E–68°E (Seyler et al., 2011; see Figure 3). The major and trace element data from peridotites from this area also have a complex history suggesting melt depletion, partly in the garnet stability field followed by an enrichment event and then followed by limited melt extraction during the recent ascent under the ridge (Seyler et al., 2011). Two of the cpxs (black patterns in Figure 3) have concave low MREE, are LREE enriched but also have the lowest Lu and Yb content. The cpx with the lowest Yb-content had to be very depleted at some point in its history, but it has $\varepsilon_{Nd} = -6.4$. The low ε_{Nd} combined with the LREE enriched pattern can only be a post-melt-depletion enrichment event, which most likely also resulted in the low ε_{Nd}. The other peridotite with a concave REE pattern with low Yb-concentration has $\varepsilon_{Hf} = 127$, while $\varepsilon_{Nd} = 11.6$ confirming both its depleted past followed by enrichment, although the TiO_2-content in the cpx is 0.02% and below detection in the spinel.

The discussion above shows that, owing to their multi-stage history of the peridotites, the chemical composition of the peridotites is complex. Assuming that high TiO_2 content of spinel indicates recent melt infiltration (Dick & Bullen, 1984), samples with elevated TiO_2 in spinel and high Hf-isotope ratios (see Figure 5) indicate that these Hf isotope ratios can be preserved, despite recent melt-rock interaction. There are four such samples with

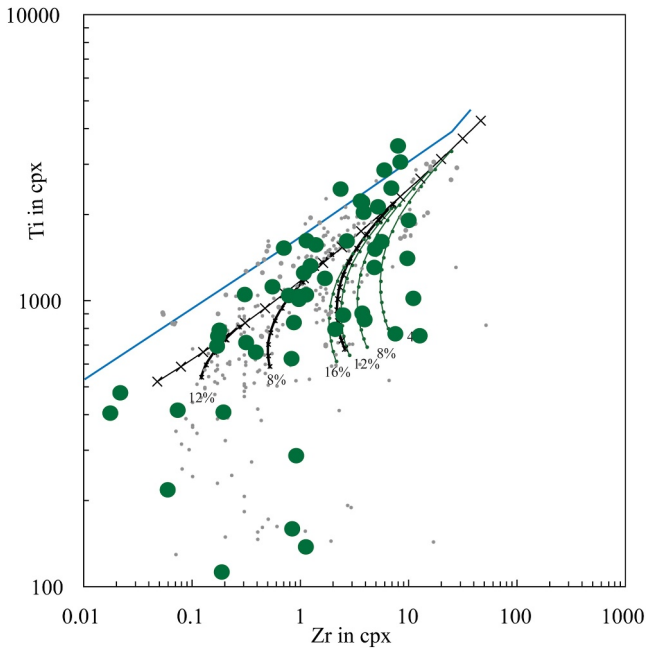

Figure 7. Cpxs from abyssal peridotite Ti and Zr contents. Green circles are cpxs east of the ABFZ on the SWIR. Gray dots are cpx data from PetDb. Depletion trends are from Mallick et al. (2014) with DMM (Salters & Stracke, 2004) as the starting composition. Black straight line is melt depletion trend resulting from fractional melting; the hatch marks are 1% increments with DM as starting compositions. Curved lines are, as described by Mallick et al. (2014), the variable depleted which are subsequently refertilized with 0.5% of melt. Different curves are for different melt compositions added. Green curves represent 0.5% addition of an aggregate melt of 4%, 8%, 12%, or 16% melting (labeled on curves) of a MORB source. Black curved lines represent 0.5% melt addition of a melt composition derived from a MORB source that has undergone 4%, 8%, or 12% fractional melting.

$\varepsilon_{Hf} > 50$ and TiO_2 in spinel >0.15 wt.% TiO_2 among the investigated Marion Rise peridotite and most prominently is sample (SMS DR08-02-08, bold green pattern in Figure 3c). This sample contains plagioclase and has spinel with 0.51 wt.% TiO_2 and Cr# of 30.3 and Mg# of 58.9, while the Mg# of the cpx is also low (0.88). The low Mg# "fits" with the high TiO_2 content and the presence of plagioclase showing the recent melt infiltration or reaction. However, the REE pattern of the sample is depleted and has $(Sm/Yb)_N$ of 0.75 and $(Ce/Sm)_N$ of 0.06, while $\varepsilon_{Hf} = 159$ and $\varepsilon_{Nd} = 4.6$. The model abundance of cpx is low <1% and cpx is not observed in the hand specimen. Additionally, the HREE content of the cpx is high with the $(Yb)_N = 5$. The high heavy REE content and the high Hf-isotopic composition indicate that the peridotite experienced melting in the garnet stability field. The low light REE content makes the residue very sensitive to resetting by a melt. Assuming that high TiO_2 and low Mg# represent the recent melt enrichment, this melt must then have been very LREE depleted before the recent melt-rock reaction. Noteworthy is that the peridotites with $TiO_2 > 0.2$ wt.% but low $(Ce/Yb)_N$ are common, which indicates the diversity of reacting melts present in the mantle (Ferrando et al., 2024; Salters & Zindler, 1995; Sanfilippo et al., 2019).

Five peridotites had cpx and an additional three had opx with unradiogenic Nd ($\varepsilon_{Nd} < 0$). The cpx, in the samples for which there is opx isotope data, have LREE depleted patterns, and low-TiO_2 spinel indicating that the isotopic composition likely represents asthenospheric sources. Peridotites with a low Nd–isotope ratio, eight in total, occur between 25°E and 65°E and as a group have few distinguishing characteristics but are all LREE depleted, all have spinels with <0.1 wt.% TiO_2 and most have high Cr# (>30). Especially peridotites from Dredge 6 of cruise SO273 have low radiogenic Nd, have less than 1% modal cpx and spinel and their bulk composition is depleted to the extent of cpx exhaustion. These samples emphasize the extreme heterogeneous nature of the asthenosphere and require a multi-stage origin that involves depletion as well as enrichment.

Summarizing, the Hf isotope ratios of the peridotites indicate an ancient high degree of melting during a previous ascent under a ridge. This depletion was overprinted by a melt rock infiltration/reaction that effected the Nd-isotope systematics more than the Hf-isotope systematics. The timing of this enrichment event is unconstrained, as is the exact composition of the metasomatizing melt. However, most abyssal peridotites at the Marion Rise have cpx with LREE depleted patterns and spinel with low Ti-content, both indicating that the peridotites are residues. Thus, the melt reaction took place prior to the recent melting during ascent under the Marion Rise. Nevertheless, there is evidence for the existence of exotic melts, or more complex histories for several peridotites that do not fit this simplified scenario, but for which an ancient depletion is still necessary.

5.2. Ancient Highly Depleted Mantle Contribution to SWIR Basalts

One would expect the high Hf-isotope ratios of the peridotites of the Marion Rise to also be present in the basalts. With the Andrew Bain Fracture zone as the western boundary, the Indian Ocean MORB have argued to have higher $^{176}Hf/^{177}Hf$ for given $^{143}Nd/^{144}Nd$ (Janney et al., 2005) similar to MORB from the Southeast Indian Ridge west of the Australian Antarctic Discordance. These MORBs also have higher $^{207}Pb/^{204}Pb$ for a given $^{206}Pb/^{204}Pb$ (Hamelin & Allègre, 1985; Hamelin et al., 1986) The high Δ7/4Pb may reflect an ancient (∼1.8 Ga) source component (Hamelin et al., 1986; Hart, 1984).

Figure 8 shows the Hf isotope ratios of the basalts as a function of longitude. Some of the ridge basalts plot well above the terrestrial array, as shown by positive $\Delta\varepsilon_{Hf}$ values up to 21.4. For comparison, the largest deviation from the terrestrial array of MORB from the Mid-Atlantic Ridge is a $\Delta\varepsilon_{Hf}$ value of 8.5. The higher and more variable $\Delta\varepsilon_{Hf}$ occur between 37°E and 50°E, where the ridge is shallowest and the Hf-isotope variation in the peridotites is large (Figure 8). Cpxs from abyssal peridotites from the Marion Rise east of the ABFZ have more

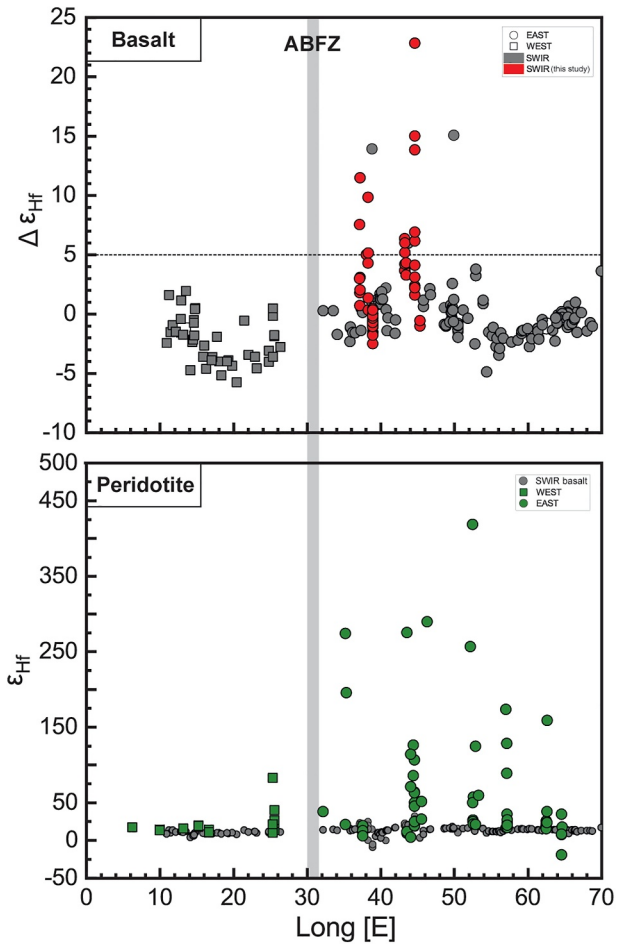

Figure 8. Hf-isotopic compositions expressed as ε_{Hf} and $\Delta\varepsilon_{Hf}$ for peridotites and basalts, respectively. $\Delta\varepsilon_{Hf}$ is the deviation of the ε_{Hf} value from the regression through the terrestrial array. A $\Delta\varepsilon_{Hf}$ higher than approximately 5 would fall outside the field for MORB and OIB. There is a clear difference in isotopic composition in both basalts and peridotites east and west of the ABFZ. Blue symbols in the basalt panel are highly vesicular basalts with extreme REE enrichment. These results show that the enrichment is not associated with radiogenic Hf isotopic composition.

variable and higher Hf isotope ratios than peridotites west of the Andrew Bain FZ. This Hf-isotope variation of the peridotites is mimicked by the isotopic compositions of the ridge basalts (Figure 8). These high $\Delta\varepsilon_{Hf}$ basalts are not remarkable in other aspects of their chemistry or isotopic compositions and are similar to other Indian Ocean MORBs. The stark contrast in variability in Hf-isotopic composition occurring in both the peridotites and the basalts shows that depleted peridotites with highly radiogenic Hf-isotope ratios contribute melt to the basalts in this section of the SWIR. The melts generated from the incompatible element depleted peridotites with high Hf isotope ratios are hard to recognize otherwise, as the incompatible trace elements were already extracted during the ancient melting event (Stracke & Bourdon, 2009). And although the peridotite solidus is affected by the amount of melt extracted (Hirschman, 2000), as long as cpx remains present, previous melted peridotite can still yield melt (Smith & Asimow, 2005; Walter & Cottrell, 2025). The Hf-isotope ratios of the Marion Rise basalts therefore show that although the peridotites are incompatible element-depleted, they can still contribute significant amounts of melt during recent melting under this part of SWIR.

However, it is unlikely that the both the Hf and the Pb isotopic signatures of the basalts are derived from the same component in a heterogeneous mantle source. A simple calculation can be made by estimating the Pb and Hf content of Marion Rise primitive basalts by calculating Pb_8 and Hf_8 values similar to Na8 values. Such a calculation shows that a 5% melt from a peridotite DM composition that was previously melted to just 3%, can contribute at most 30% of the Pb-budget of a primitive SWIR MORB, whereas more than 60% of the Hf budget can be provided by the melt of this depleted peridotite (see also Stracke & Bourdon, 2009). The remainder of the trace element budget has to be supplied by an enriched component, most likely some form of recycled oceanic crust. Therefore, the Pb and the Hf signature of Indian MORB is influenced to different extends by different components of a heterogeneous mantle. The high ΔεHf values in Indian MORB reflect a contribution from an ancient highly depleted peridotite, whereas most of the Pb is supplied from minor incompatible element enriched components. The coincidence of the Pb and Hf isotope variations can be explained if east of the Andrew Bain Fracture Zone the peridotite has higher Hf isotope ratios and is more incompatible element depleted than the peridotites to the west of the ABFZ. In this case, the lower Pb contents of the Marion Rise peridotites make their melt Pb-isotopic composition more susceptible to modification by melts from incompatible element enriched source components.

5.3. Can Depleted Mantle Support the Marion Rise?

Peridotites recovered from the Marion Rise have high Hf -isotope ratios and show the presence of a highly depleted mantle beneath the Rise. This highly depleted signature is also reflected in the basalts (see Figure 8) and both basalts and peridotites have higher Hf-isotope ratios than those from west of the Andrew Bain Fracture Zone. Additionally, the basalts over the Marion Rise have low Na8 and Ti8 (Figure S3 in Supporting Information S1), especially given the absent or thin crust over the Rise and abundant peridotite exposures. The thin crust at the Marion Rise ridge (Zhou & Dick, 2013) indicates that this oceanic rise is not the result of higher mantle potential temperature with associated excess melting and thick oceanic crust. Instead, it has been argued that the ocean rise can be sustained by buoyant, melt-depleted mantle (Niu & O'Hara, 2008; Zhou & Dick, 2013) as melt depletion will decrease the density of the residual peridotite (Afonso & Schutt, 2012; Schutt & Lesher, 2006).

However, it is difficult to estimate the extent of the mantle depletion and density prior to recent melting from the abyssal peridotites, because it is difficult to estimate how much melt has been extracted from each sampled peridotite during recent ascent under the SWIR. For example, expedition TN365 retrieved 633 kg of mantle rocks

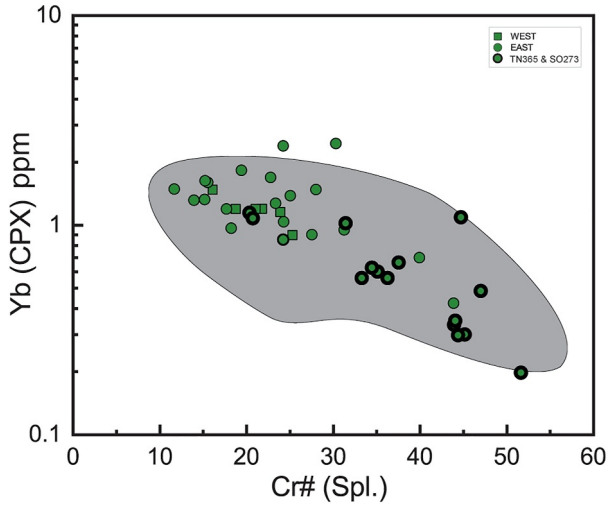

Figure 9. Yb content in cpx versus Cr# in spinel after (Warren, 2012). Gray symbols represent the compilation of Warren (2012). This figure shows that the SO273 and TN365 data fall at the depleted end of the spectrum of abyssal peridotites and thus provide further evidence for the depleted character of the mantle beneath the Marion Rise.

from the ocean floor of which 60% was identified as peridotite with model cpx generally less than 10% and 40% identified as dunite or ultramafic mylonite with only trace amounts of cpx, that is, mantle that has undergone larger depletion than the analyzed peridotites.

Walter and Cottrell (2025) showed that melt productivity of peridotite does not decrease significantly until one gets close to cpx being exhausted, which is at a minimum of 15% melting. Most of the peridotites analyzed in this study retained at least several percent of cpx, but nevertheless experienced high degrees of melt depletion, as evidenced by their; the modal cpx abundance (Dick & Fisher, 1984), the Cr# in spinel (Dick & Bullen, 1984; Hellebrand et al., 2001), and the REE pattern in the cpx as well as its HREE content. Moreover, the Cr# in spinel versus Yb diagram (Figure 9) shows that the peridotites from expeditions TN365 and SO273 that sampled the shallower part of the Marion Rise fall on the depleted end of the spectrum of abyssal peridotites in general (Warren, 2012). The individual peridotites are highly variable, however, and it is difficult to extract an average extent of melt depletion prior to the recent melting under the ridge, especially considering that the abyssal peridotites represent just the uppermost part of the sub-ridge asthenosphere.

Having established that the mantle beneath the Marion Rise is at the depleted end of the spectrum, what magnitude of depletion is required to support the height difference of the Rise compared to normal ridge depth of 3,000 m (Schilling, 1975) or average ridge depth of the ridge west of the Andrew Bain Fracture Zone of 3,700 m (Gale et al., 2014)? The average ridge depth over the top of the Marion Rise is approximately 2,000 m, although the shallowest depth encountered is 850 m, which we assume is free of crust. Away from the Marion Rise, a "model ridge" depth profile would have the ocean floor at 3,000 m, 3 km of basalt/diabase ($\rho = 3{,}000$ kg·m^{-3}) and 3 km of gabbro ($\rho = 3{,}300$ kg·m^{-3}), below which there is peridotite ($\rho = 3{,}300$ kg·m^{-3}). Assuming the Rise is the result of reduced density of the upper 200 km, this would require 0.5% reduction in density compared to the adjacent asthenosphere. Melt depletion of peridotite has been modeled by Afonso and Schutt (2012) as $\delta\rho = -214.5$ F with ρ being density in (kg·m^{-3}) and F being the fraction of melt removed. With these numbers, approximately 7% of melting is required to decrease the peridotite density by 0.5%. This is a relatively small difference in the level of depletion between "normal" ridge and the Marion Rise. This exercise shows that the type of differences in mantle depletion is within the range of composition one can expect from variably melt depleted peridotite. Most likely, the majority of the peridotitic mantle is heterogeneous and more melt and incompatible element depleted than bulk sub-ridge mantle calculated from inversion of incompatible trace element contents of MORB (Stracke & Salters, 2025; Workman & Hart, 2005).

6. Conclusion

The presented large data set of Nd-Hf-isotope ratios of abyssal peridotites confirms the ubiquitous presence of ancient, highly incompatible element-depleted peridotites in the sub-ridge mantle. The isotopic characteristics of the SWIR peridotites –high Hf isotope ratios ranging to values up to $\varepsilon_{Hf} = +417$ (total range of ε_{Hf} from −19 to +417) at a much more restricted range of Nd isotope ratios (ε_{Nd} of −18 to +93)—require a complex history of ancient melt depletion, possibly dating back to at least 1 Ga and likely 3.0–3.5 Ga for the most extreme isotopic compositions, followed by addition of a melt with significant higher Nd/Hf, before the peridotite melted again during recent ascent under the SWIR.

The extreme Hf-isotope ratios of the peridotites contrast with the far more restricted range of values west of the Andrew Bain Fracture Zone. The Hf-Nd systems in the basalts of the SWIR east of the Andrew Bain Fracture Zone with high $\Delta\varepsilon_{Hf}$ mimic the geographic pattern of the peridotites, which indicates that melts from peridotites with high Hf-isotope ratios have contributed a significant part of the incompatible element budget to the basalts.

The extreme Hf-isotopic compositions of the Marion Rise peridotites are further evidence that the Marion Rise is supported by low density asthenosphere as a result of a depleted composition instead of excess temperature.

Peridotites with high TiO_2 in spinel, which indicates recent melt addition, still have high Hf-isotope ratios and are evidence of the presence of melts with decoupled Hf and Nd-isotope systems in the sub-ridge mantle. Additionally, LREE depleted peridotites with low Nd-isotopic composition add to the picture of extreme heterogeneity of the Marion Rise sub-ridge mantle.

The Andrew Bain Fracture Zone is a major divide between two mantle provinces with distinct compositions of the exposed abyssal peridotites and ridge basalts. West of the Andrew Bain Fracture ZoneZ, both basalts and peridotites show limited variation in Hf-isotopic composition, while on the Eastern side of the Andrew Bain Fracture Zone, both basalts and peridotites have more radiogenic and more variable Hf-isotopic compositions. This radiogenic Hf-signature is typical for the Indian Ocean mantle domain and is related to depleted peridotite and thus has another origin than the Pb isotope difference.

Data Availability Statement

All data in Tables 1 and 2 and S2 are available in Earthchem Woelki and Salters (2025). Additional SWIR data is archived at Wang et al. (2025). The data for the Gakkel Ridge is archived at (Salters, 2025).

Acknowledgments
We thank Afi Sachi Kocher for help during sample preparation. We would also like to thank the crew and scientists of RV Thomas G. Thompson TN365 cruise and the Sonne SO273 cruise. The cruise was supported by the US National Science Foundation, with additional support from Tongji University, Shanghai China and the Deutsche Forschungs Gemeinschaft: Federal Ministry of Education and Research (BMBF) Project Number: 03G0273E. We acknowledge funding from NSF grants OCE-1657826, OCE-2126496 (to V.J.M.S.) and DMR-2128556. Part of this work was performed at the National High Magnetic Field Laboratory, which is supported by NSF Cooperative Agreement no. DMR-1157490 and DMR-1644779 and the state of Florida. Lastly, we very much appreciate the comments of two anonymous reviewers, which significantly improved the manuscript.

References

Afonso, J. C., & Schutt, D. L. (2012). The effects of polybaric partial melting on density and seismic velocities of mantle restites. *Lithos*, *134–135*, 289–303. https://doi.org/10.1016/j.lithos.2012.01.009

Beier, C., Brandl, P. A., Lima, S. M., & Haase, K. M. (2018). Tectonic control on the genesis of magmas in the New Hebrides arc (Vanuatu). *Lithos*, *312–313*, 290–307. https://doi.org/10.1016/j.lithos.2018.05.011

Birner, S. K., Warren, J. M., Cottrell, E., Davis, F. A., Kelley, K. A., & Falloon, T. J. (2017). Forearc peridotites from Tonga record heterogeneous oxidation of the mantle following subduction initiation. *Journal of Petrology*, *58*(9), 1755–1780. https://doi.org/10.1093/petrology/egx072

Brunelli, D., Cipriani, A., & Bonatti, E. (2018). Thermal effects of pyroxenites on mantle melting below mid-ocean ridges. *Nature Geoscience*, *11*(7), 520–525. https://doi.org/10.1038/s41561-018-0139-z

Brunelli, D., Paganelli, E., & Seyler, M. (2014). Percolation of enriched melts during incremental open-system melting in the spinel field: A REE approach to abyssal peridotites from the Southwest Indian Ridge. *Geochimica et Cosmochimica Acta*, *127*, 190–203.

Brunelli, D., Seyler, M., Cipriani, A., Ottolini, L., & Bonatti, E. (2006). Discontinuous melt extraction and weak refertilization of mantle peridotites at the Vema lithospheric section (Mid-Atlantic Ridge). *Journal of Petrology*, *47*(4), 745–771. https://doi.org/10.1093/petrology/egi092

Chauvel, C., Lewin, E., Carpentier, M., Arndt, N. T., & Marini, J.-C. (2008). Role of recycled oceanic basalt and sediment in generating the Hf–Nd mantle array. *Nature Geoscience*, *1*, 64–67. https://doi.org/10.1038/ngeo.2007.51

Cipriani, A., Brueckner, H., Bonatti, E., & Brunelli, D. (2004). Oceanic crust generated by elusive parents: Sr and Nd isotopes in basalt-peridotite pairs from the Mid-Atlantic Ridge. *Geology*, *32*(8), 657–660. https://doi.org/10.1130/g20560.1

Dick, H. J. B., & Bullen, T. D. (1984). Chromian spinel as a petrogenetic indicator in abyssal and alpine-type peridotite and spatially associated lavas. *Contributions to Mineralogy and Petrology*, *86*(1), 54–76. https://doi.org/10.1007/bf00373711

Dick, H. J. B., & Fisher, R. L. (1984). Mineralogical studies of the residuals of mantle melting: Abyssal and alpine-type peridotites. In J. Kornprobst (Ed.), *Kimberlites II: The mantle and crust-mantle relationships* (pp. 295–308). Elsevier.

Dick, H. J. B., Fisher, R. L., & Bryan, W. B. (1984). Mineralogical variability of the uppermost mantle along mid-ocean ridges. *Earth and Planetary Science Letters*, *69*, 88–106.

Dupré, B., & Allègre, C. J. (1983). Pb-Sr isotope variation in Indian Ocean and mixing phenomena. *Nature*, *303*(5913), 142–146. https://doi.org/10.1038/303142a0

Ferrando, C., Borghini, G., Sani, C., Genske, F., Ligi, M., Stracke, A., & Sanfilippo, A. (2024). Deep segregation and crystallization of ultra-depleted melts in the sub-ridge mantle. *Chemical Geology*, *644*, 121840. https://doi.org/10.1016/j.chemgeo.2023.121840

Fisher, R. L., Dick, H. J. B., Natland, J. H., & Meyer, P. S. (1984). Mafic/ultramafic suites of the slowly spreading southwest Indian ridge: Protea exploration of the Antarctic plate boundary, 24°E–47°E, 1984. *Ophioliti*, *11*, 147–178.

Gale, A., Langmuir, C. H., & Dalton, C. A. (2014). The global systematics of ocean ridge basalts and their origin. *Journal of Petrology*, *55*(6), 1051–1082. https://doi.org/10.1093/petrology/egu017

Gale, A. S., Dalton, C. A., Langmuir, C. H., Su, Y. J., & Schilling, J.-G. (2013). The mean composition of ocean ridge basalts. *Geochemistry, Geophysics, Geosystems*, *14*(3), 489–518. https://doi.org/10.1029/2012gc004334

Gao, C., Dick, H. J. B., Liu, Y., & Zhou, H. (2016). Melt extraction and mantle source at a Southwest Indian Ridge Dragon Bone amagmatic segment on the Marion Rise. *Lithos*, *246–247*, 48–60. https://doi.org/10.1016/j.lithos.2015.12.007

Hamelin, B., & Allègre, C. J. (1985). Large-scale regional units in the depleted upper mantle revealed by an isotope study of the South-West Indian Ridge. *Nature*, *315*(6016), 196–199. https://doi.org/10.1038/315196a0

Hamelin, B., Dupré, B., & Allègre, C. J. (1986). Pb-Sr-Nd isotopic data of Indian Ocean Ridges: New evidence of large scale mapping of mantle heterogeneities. *Earth and Planetary Science Letters*, *76*, 288–298.

Hart, S. R. (1984). A large-scale isotope anomaly in the Southern Hemisphere mantle. *Nature*, *309*(5971), 753–757. https://doi.org/10.1038/309753a0

Hellebrand, E., Snow, J. E., Dick, H. J. B., & Hofmann, A. W. (2001). Coupled major and trace elements as indicators of the extent of melting in mid-ocean-ridge peridotites. *Nature*, *410*(6829), 677–681. https://doi.org/10.1038/35070546

Hirschman, M. M. (2000). Mantle solidus: Experimental constraints and the effects of peridotite composition. *Geochemistry, Geophysics, Geosystems*, 2000GC000070.

Humler, E. (2001). MD 121/SWIFT cruise, RV Marion Dufresne.

Janney, P. E., Le Roex, A. P., & Carlson, R. W. (2005). Hafnium isotope and trace element constraints on the nature of mantle heterogeneity beneath the Central Southwest Indian Ridge (13°E to 47°E). *Journal of Petrology*, *46*(12), 2427–2464. https://doi.org/10.1093/petrology/egi060

Johnson, K. T. M., Dick, H. J. B., & Shimizu, N. (1990). Melting in the oceanic upper mantle: An ion microprobe study of diopsides in abyssal peridotites. *Journal of Geophysical Research*, *95*(B3), 2661–2678. https://doi.org/10.1029/jb095ib03p02661

Jones, R. E., van Keken, P. E., Hauri, E. H., Tucker, J. M., Vervoort, J. D., & Ballentine, C. J. (2019). Origins of the terestrial Hf-Nd array: Evidence from a combined geodynamical-geochemical approach. *Earth and Planetary Science Letters*, *518*, 26–39. https://doi.org/10.1016/j.epsl.2019.04.015

Klein, E. M., & Langmuir, C. H. (1987). Global correlations of ocean ridge basalt chemistry with axial depth and crustal thickness. *Journal of Geophysical Research*, *92*(B8), 8089–8115. https://doi.org/10.1029/jb092ib08p08089

Longhi, J. (2002). Some phase equilibria systematics of lherzolite melting: I. *Geochemistry, Geophysics, Geosystems*, *3*, GC000204. https://doi.org/10.1029/2001GC000204

Mahoney, J., Le Roex, A. P., Peng, Z., Fisher, R. L., & Natland, J. H. (1992). Southwestern limits of Indian Ocean Ridge mantle and the origin of low $^{206}Pb/^{204}Pb$ mid-ocean ridge basalt: Isotope systematics of the Central Southwest Indian Ridge (17-50E). *Journal of Geophysical Research*, *97*(B13), 19771–719790. https://doi.org/10.1029/92jb01424

Mallick, S., Dick, H. J. B., Sachi-Kocher, A., & Salters, V. J. M. (2014). Isotope and trace element insights into heterogeneity of subridge mantle. *Geochemistry, Geophysics, Geosystems*, *15*(6), 2438–2453. https://doi.org/10.1002/2014gc005314

Mallick, S., Standish, J. J., & Bizimis, M. (2015). Constraints on the mantle mineralogy of an ultra-slow ridge: Hafnium isotopes in abyssal peridotites and basalts from the 9–25°E Southwest Indian Ridge. *Earth and Planetary Science Letters*, *410*, 42–53. https://doi.org/10.1016/j.epsl.2014.10.048

McDonough, W. F., & Sun, S.-s. (1995). The composition of the Earth. *Chemical Geology*, *120*(3–4), 223–253. https://doi.org/10.1016/0009-2541(94)00140-4

Meyzen, C. M., Blichert-Toft, J., Ludden, J. N., Humler, E., Mevel, C., & Albarede, F. (2007). Isotopic portrayal of the Earth's upper mantle flow field. *Nature*, *447*(7148), 1069–1074. https://doi.org/10.1038/nature05920

Meyzen, C. M., Ludden, J. N., Humler, E., Luais, B., Toplis, M. J., Mevel, C., & Storey, M. (2005). New insights into the origin and distribution of the DUPAL isotope anomaly in the Indian Ocean mantle from MORB of the Southwest Indian Ridge. *Geochemistry, Geophysics, Geosystems*, *6*(11), Q11K11. https://doi.org/10.1029/2005gc000979

Morgan, W. J. (1971). Convection plumes in the lower mantle. *Nature*, *230*(5288), 42–43. https://doi.org/10.1038/230042a0

Morgan, W. J. (1972). Plate motions and deep mantle convection. *Geological Society of America Memoir*, *132*, 7–22. https://doi.org/10.1130/mem132-p7

Niu, Y., & O'Hara, M. J. (2008). Global correlations of ocean ridge basalt chemistry with axial depth: A new perspective. *Journal of Petrology*, *49*, 633–664.

O'Hara, M. J. (1965). Primary magmas and the origin of basalts. *Scottish Journal of Geology*, *1*, 19–40. https://doi.org/10.1144/sjg01010019

O'Neill, H. Ct. C., & Jenner, F. E. (2016). Causes of the compositional variability among ocean floor basalts. *Journal of Petrology*, *57*(11–12), 2163–2194.

Paquet, M., Hamelin, C., Moreira, M., & Cannat, M. (2020). The isotopic (He, Ne, Sr, Nd, Hf, Pb) signature in the Indian Mantle over 8.8 Ma. *Chemical Geology*, *550*, 119741. https://doi.org/10.1016/j.chemgeo.2020.119741

Patriat, P., & Segoufin, J. (1988). Reconstruction of the central Indian Ocean. *Tectonophysics*, *155*(1–4), 211–223. https://doi.org/10.1016/0040-1951(88)90267-3

Pearce, J. A., Kempton, P. D., Nowell, G. M., & Noble, S. R. (1999). Hf-Nd element and isotope perspective on the nature and provenance of mantle and subduction components in Western Pacific Arc- Basin systems. *Journal of Petrology*, *40*(11), 1579–1611. https://doi.org/10.1093/petroj/40.11.1579

Presnall, D., & Helsley, C. (1982). Physics of the Earth and Planetary interiors, 29(2): 148-160 (1982) Diapirism of depleted peridotite—A model for the origin of hot spots. *Physics of the Earth and Planetary Interiors*, *29*(2), 148–160. https://doi.org/10.1016/0031-9201(82)90069-3

Salters, V. J. M. (2025). Isotopic composition of Gakkel Ridge peridotites. *Interdisciplinary Earth Data Alliance (IEDA)*. https://doi.org/10.60520/IEDA/113797

Salters, V. J. M., & Dick, H. J. B. (2002). Mineralogy of the mid-ocean ridge basalt source from neodymium isotopic composition in abyssal peridotites. *Nature*, *418*(6893), 68–72. https://doi.org/10.1038/nature00798

Salters, V. J. M., & Dick, H. J. B. (2011). Ultra depleted mantle at the Gakkel Ridge based on Hafnium and Neodymium isotopes. In *Eos Trans. AGU* (p. V41G-02).

Salters, V. J. M., Longhi, J., & Bizimis, M. (2002). Near mantle solidus trace element partitioning at pressures up to 3.4 GPa. *Geochemistry, Geophysics, Geosystems*, *3*(7), 2001GC000148. https://doi.org/10.1029/2001gc000148

Salters, V. J. M., & Longhi, J. E. (1999). Trace element partitioning during the initial stages of melting beneath ocean ridges. *Earth and Planetary Science Letters*, *166*(1–2), 15–30. https://doi.org/10.1016/s0012-821x(98)00271-4

Salters, V. J. M., & Stracke, A. (2004). The composition of the depleted mantle. *Geochemistry, Geophysics, Geosystems*, *5*, 2003GC000597. https://doi.org/10.1029/2003gc000597

Salters, V. J. M., & Zindler, A. (1995). Extreme $^{176}Hf/^{177}Hf$ in the sub-oceanic mantle. *Earth and Planetary Science Letters*, *129*(1–4), 13–30. https://doi.org/10.1016/0012-821x(94)00234-p

Sanfilippo, A., Salters, V. J. M., Tribuzio, R., & Zanetti, A. (2019). Ultra-depleted melt from an ancient, refractory oceanic mantle. *Earth and Planetary Science Letters*, *511*, 89–99.

Sanfilippo, A., Stracke, A., Genske, F., scarani, S., Cuffaro, M., Basch, V., et al. (2024). Upwelling of melt-depleted mantle under Iceland. *Nature Geoscience*, *17*(10), 1046–1052. https://doi.org/10.1038/s41561-024-01532-z

Sani, C., Sanfilippo, A., Ferrando, C., Sergey, A. A., Skolotonev, S. G., Muccini, F., et al. (2020). Ultra-depleted melt refertilization of mantle peridotites in a large intra-transform domain (Doldrums Fracture Zone; 7–8°N, Mid Atlantic Ridge). *Lithos*, 374–375.

Sani, C., Sanfilippo, A., Peyve, A. A., Genske, F., & Stracke, A. (2023). Earth Mantle's isotopic record of progressive chemical depletion. *AGU ADvances*, *4*(2), e2022AV000792. https://doi.org/10.1029/2022av000792

Sani, C., Sanfilippo, A., Skolotev, S., Ligi, M., Genske, F., & Stracke, A. (2024). Sampling Earth's mantle at intra-transform spreading ridges. *Geochimica et Cosmochimica Acta*, *2024*, 156–172.

Sani, R. K., Peyton, B. M., Amonette, J. E., & Geesey, G. G. (2004). Reduction of uranium (VI) under sulfate-reducing conditions in the presence of Fe (III)-(hydr)oxides. *Geochimica et Cosmochimica Acta*, *68*(12), 2639–2648. https://doi.org/10.1016/j.gca.2004.01.005

Sauter, D., & Cannat, M. (2010). The ultraslow spreading Southwest Indian Ridge. In P. A. Rona, C. W. Devey, J. Dyment, & B. Murton (Eds.), *Diversity of hydrothermal systems on slow spreading ocean ridges* (pp. 153–173). AGU.

Sauter, D., Cannat, M., Rouméjon, S., Andreani, M., Birot, D., Bronner, A., et al. (2013). Continuous exhumation of mantle-derived rocks at the Southwest Indian Ridge for 11 million years. *Nature Geoscience*, *6*(4), 314–320. https://doi.org/10.1038/ngeo1771

Schilling, J.-G. (1975). Rare-earth variations across 'normal segments' of the Reykjanes Ridge, 60°-53°N, Mid-Atlantic Ridge, 29°S, and East Pacific Rise, 2°-19°S, and evidence on the composition of the underlying low-velocity layer. *Journal of Geophysical Research*, *80*(11), 1459–1473. https://doi.org/10.1029/jb080i011p01459

Schutt, D. L., & Lesher, C. E. (2006). Effects of melt depletion on the density and seismic velocity of garnet and spinel lherzolite. *Journal of Geophysical Research*, *111*(B5), B05401. https://doi.org/10.1029/2003jb002950

Seyler, M., Brunelli, D., Toplis, M. J., & Cannat, M. (2011). Multiscale chemical heterogeneities beneath the eastern Southwest Indian Ridge (52°E–68°E): Trace element compositions of along-axis dredged peridotites. *Geochemistry, Geophysics, Geosystems*, *12*(9), Q0AC15. https://doi.org/10.1029/2011gc003585

Seyler, M., Cannat, M., & Mével, C. (2003). Evidence for major-element heterogeneity in the mantle source of abyssal peridotites from the Southwest Indian Ridge (52° to 68°E). *Geochemistry, Geophysics, Geosystems*, *4*(2). https://doi.org/10.1029/2002GC000305

Seyler, M., Lorand, J. P., Dick, H. J. B., & Drouin, M. (2007). Pervasive melt percolation reactions in ultra-depleted refractory harzburgites at the Mid-Atlantic Ridge, 15 degrees 20'N: ODP Hole 1274A. *Contributions to Mineralogy and Petrology*, *153*(3), 303–319. https://doi.org/10.1007/s00410-006-0148-6

Smith, P. M., & Asimow, P. D. (2005). Adiabat_1ph: A new public front-end to the MELTS, pMELTS, and pHMELTS models. *Geochemistry, Geophysics, Geosystems*, *6*(2), Q02004. https://doi.org/10.1029/2004gc000816

Standish, J. J., Hart, S. R., Blusztajn, J., Dick, H. J. B., & Lee, K. L. (2002). Abyssal peridotite osmium isotopic compositions from Cr-spinel. *Geochemistry, Geophysics, Geosystems*, *3*(1), 1–24. https://doi.org/10.1029/2001GC000161

Stracke, A. (2021). A process-oriented approach to mantle geochemistry. *Chemical Geology*, *579*, 120350. https://doi.org/10.1016/j.chemgeo.2021.120350

Stracke, A., & Bourdon, B. (2009). The importance of melt extraction for tracing mantle heterogeneity. *Geochimica et Cosmochimica Acta*, *73*(1), 218–238. https://doi.org/10.1016/j.gca.2008.10.015

Stracke, A., & Salters, V. J. M. (2025). The role of peridotite for oceanic volcanism. *Geochemistry, Geophysics, Geosystems*, *26*(8), e2025GC012463. https://doi.org/10.1029/2025gc012463

Stracke, A., & Snow, J. E. (2009). The Earth's mantle is more depleted than we thought. *Eos Trans Am Geophys Un*, *90*, V24A-03.

Stracke, A., Snow, J. E., Hellebrand, E., von der Handt, A., Bourdon, B., Birbaum, K., & Günther, D. (2011). Abyssal peridotite Hf isotopes identify extreme mantle depletion. *Earth and Planetary Science Letters*, *308*(3–4), 359–368. https://doi.org/10.1016/j.epsl.2011.06.012

Stracke, A., Willig, M., Genske, F., Beguelin, P., & Todd, E. (2022). Chemical Geodynamics insights from a machine learning approach. *Geochemistry Geophysics Geosystems*, *23*, e2022GC010606.

Stracke, A., Zindler, A., Salters, V. J. M., McKenzie, D. E., & Grönvold, K. (2003). The dynamics of melting beneath Theistareykir, northern Iceland. *Geochemistry, Geophysics, Geosystems*, *4*(10), 2002GC000347. https://doi.org/10.1029/2002gc000347

Vervoort, J. D., & Blichert-Toft, J. (1999). Evolution of the depleted mantle: Hf isotope evidence from juvenile rocks through time. *Geochimica et Cosmochimica Acta*, *63*(3–4), 533–556. https://doi.org/10.1016/s0016-7037(98)00274-9

Vervoort, J. D., Plank, T., & Prytulak, J. (2011). The Hf–Nd isotopic composition of marine sediment. *Geochimica et Cosmochimica Acta*, *75*(20), 5903–5926. https://doi.org/10.1016/j.gca.2011.07.046

Walter, M., & Cottrell, E. (2025). Equilibrium constraints on partial melting in the upper mantle. In *Treatise in geochemistry* (3rd ed. ed, pp. 231–273).

Wang, J., Zhou, H., & Salters, V. J. M. (2025). Isotopic composition of abyssal peridotites from 53°E SWIR, Version 1.0. Interdisciplinary Earth Data Alliance (IEDA). https://doi.org/10.60520/IEDA/113818

Wang, J., Zhou, H., Salters, V. J. M., Dick, H. J. B., Standish, J. J., & Wang, C. (2020). Trace element and isotopic evidence for recycled lithosphere at basalts from 48°E to 53°E, Southwest Indian Ridge. *Journal of Petrology*, *61*(10), egaa068. https://doi.org/10.1093/petrology/egaa068

Warren, J. M. (2012). Global variations in abyssal peridotite compositions. *Lithos*, *248–251*, 193–219. https://doi.org/10.1016/j.lithos.2015.12.023

Warren, J. M., & Shimizu, N. (2010). Cryptic variations in abyssal peridotite compositions: Evidence for shallow-level melt infiltration in the oceanic lithosphere. *Journal of Petrology*, *51*(1–2), 395–423. https://doi.org/10.1093/petrology/egp096

Woelki, D., Haase, K. M., Schoenhofen, M. V., Beier, C., Regelous, M., Krumm, S. H., & Günther, T. (2018). Evidence for melting of subducting carbonate-rich sediments in the western Aegean Arc. *Chemical Geology*, *483*, 463–473. https://doi.org/10.1016/j.chemgeo.2018.03.014

Woelki, D., & Salters, V. (2025). Major element, trace element, and isotope data of mineral separates from abyssal peridotites and basalts from the Eastern part of the South West Indian Ridge v.2, Version 1.0. *Interdisciplinary Earth Data Alliance (IEDA)*. https://doi.org/10.60520/IEDA/114002

Woelki, D., Salters, V. J. M., Beier, C., Dick, H. J. B., Koepke, J., & Romer, R. L. (2023). Shallow recycling of lower continental crust: The Mahoney Seamount at the Southwest Indian Ridge. *Earth and Planetary Science Letters*, *602*, 117968. https://doi.org/10.1016/j.epsl.2022.117968

Workman, R. K., & Hart, S. R. (2005). Major and trace element composition of the depleted MORB mantle (DMM). *Earth and Planetary Science Letters*, *231*(1–2), 53–72. https://doi.org/10.1016/j.epsl.2004.12.005

Zanetti, A., D'Antonio, M., Spadea, P., Raffone, N., Vannucchi, R., & Bruguier, O. (2006). Petrogenesis of Mantle peridotites from the Izu-Bonin Mariana (IBM) forearc. *Ophioliti*, *31*, 189–206.

Zhang, W.-Q., Liu, C.-Z., Dick, H. J. B., Mitchell, R., & Liu, B.-d. (2024). Oceanic mantle beneath ultraslow spreading ridges metasomatized by variably evolved melts. *Contributions to Mineralogy and Petrology*, *179*(2), 15. https://doi.org/10.1007/s00410-023-02093-x

Zhou, H., & Dick, H. J. B. (2013). Thin Crust as evidence for depleted mantle supporting the Marion Rise. *Nature*, *494*(7436), 195–200. https://doi.org/10.1038/nature11842